Internal Processes Driving the Slow-to-Fast Transition of a Rockslide

Sibashish Dash[1,2], Michael Dietze[3], Qi Zhou[1], Jens M. Turowski[1], Peter Makus[1], Fabian Walter[4], Marcel Fulde[5], Niels Hovius[1,2]

[1]GFZ Helmholtz Centre for Geosciences, Potsdam, 14473, Germany
[2]Institute of Geosciences, University of Potsdam, Potsdam, Germany
[3]Georg-August-University Göttingen, Göttingen, Germany
[4]Swiss Federal Institute for Forest, Snow and Landscape Research WSL, Birmensdorf, Switzerland
[5]Geo Inventure, Häuslerstrasse 52, CH-8800 Thalwil, Switzerland

This manuscript is a non-peer-reviewed preprint submitted to EarthArXiv. The manuscript may undergo additional revision prior to journal submission or publication.

Corresponding author: Sibashish Dash, dash@gfz.de

Abstract

Landslides may creep slowly for decades to centuries under external influences such as rainfall or seismic shaking. Predicting when and how they transition into catastrophic acceleration remains a major challenge because the internal processes driving failure occur at depth and are often not evident from surface observations alone. Here, we combine local seismic and geodetic measurements to investigate landslide dynamics during the final 55 days preceding the collapse of the 2-million-m^3 Brienz/Brinzauls rockslide (Switzerland) in summer 2023. Using a supervised machine-learning approach applied to continuous seismic data, we detect and classify subsurface cracking and rockfalls within the accelerating slope and track their temporal evolution. Initially both cracking and rockfall activity were primarily rainfall-driven. However, 37 days before collapse, we identify the onset of runaway acceleration, marked by an increase in subsurface cracking despite the absence of rainfall. Seismic observations further indicate a progressive increase in the efficiency of basal sliding that persisted until failure. In contrast, rockfall activity responded about 8 days later, reflecting progressive degradation of the mechanical integrity of the moving mass, with the surface-to-subsurface event ratio showing a pronounced increase during the final three days before failure. These observations resolve the coupled evolution of the basal shear zone and the deforming rock mass leading up to catastrophic failure. Our results demonstrate that internal damage processes alone can sustain runaway acceleration for more than a month, even in the absence of significant rainfall, revealing fundamental slow-to-fast transition mechanics previously inferred mainly from laboratory experiments and physical models, opening new avenues for advancing future early warning approaches.

Key Points:

- Seismic monitoring captured the slow-to-fast transition of the Brienz/Brinzauls rockslide.
- Runaway acceleration toward failure was marked by increasingly efficient sliding relative to seismic activity.
- Seismic observations of basal slip and internal damage processes show potential for landslide early warning.

Plain Language Summary

In summer 2023, the Swiss village of Brienz/Brinzauls narrowly escaped a disaster when a massive rockslide stopped just short of the village. The behavior of the rockslide became highly difficult to anticipate in the weeks preceding failure. Using seismic sensors, we tracked fractures deep within the mountain and surface rockfalls tumbling down the slope. Early on, rainfall controlled the slope's movement, but about 37 days before collapse, seismic activity revealed growing internal instability and a progressive loss of resistance to sliding, allowing the slope to accelerate even without rainfall. Surface rockfalls surged a few days later, and the slope eventually fragmented into an intense cascade of debris, marking the culmination of the event. The slow-to-fast transition observed in Brienz/Brinzauls is a key process governing the onset of runaway acceleration and is therefore critical for the development of reliable early-warning systems.

1 Introduction

Slope failures often occur abruptly and with little warning, causing loss of life (Froude & Petley, 2018; Petley, 2012) and extensive material damage (Kjekstad & Highland, 2009;

Dilley et al., 2012). They can trigger cascading hazards that propagate far beyond the initial source, transport, and deposition zones (Sattar et al., 2025; Cook et al., 2021). Increasing population pressure (Ehrlich et al., 2021), together with changes in hydrosphere (Kirschbaum et al., 2020) and cryosphere (Patton et al., 2019), are further amplifying these risks. Despite decades of methodological advances in forecasting and risk mitigation, the anticipation of catastrophic slope failure remains a major scientific challenge (Intrieri et al., 2019), fundamentally limited by our ability to resolve and quantify the complex deformation processes occurring at depth.

At depth, rock-slope failure initiates through the nucleation, propagation, and coalescence of cracks under critical to subcritical stress conditions (Brantut et al., 2013a; Voigtländer et al., 2018). Progressive damage localization eventually forms a rupture surface that detaches a rock volume from the surrounding rock. Once detached, the unstable mass may enter a phase of slow mobilization expressed as creeping, sliding, or toppling along the rupture plane (Hungr et al., 2014). This mobilization arises under gravity, through the interplay between external forcing mechanisms—such as seismic shaking, thermal stressing, and hydraulic pore-pressure variations (Bontemps et al., 2020; Lombardo et al., 2019; Zhang et al., 2024; Loche et al., 2022; Gischig et al., 2011; H. F. Wang et al., 1989; Finnegan et al., 2021; Carey et al., 2019)—and the evolving internal state of the slope, including progressive fragmentation of the rock mass and changes in basal frictional properties (Agliardi et al., 2020a; Noël et al., 2023b; Paul et al., 2024b). Despite being three-dimensional bodies, most numerical modelling and laboratory studies interpret slow-to-fast landslide transitions in terms of either the nucleation of a basal shear plane or frictional processes operating along it. (e.g., Handwerger et al., 2016a; Paul et al., 2024b; Helmstetter et al., 2004; C. R. Kilburn & Petley, 2003; Sornette et al., 2004; Agliardi et al., 2020a; Ferri et al., 2011; Chang et al., 2024). Lithological variation within the mass, spatially heterogeneous deformation, and evolving rupture geometries challenge idealized models and limit the transferability of mechanistic insights, underscoring the need to resolve the coupled evolution of basal slip, and bulk fragmentation (Faillettaz et al., 2010b).

Under sustained load, pre-failure deformation is commonly divided into primary, secondary, and tertiary creep stages, which exhibit decelerating, steady-state, and accelerating strain rates, respectively (Intrieri et al., 2019). Prior to tertiary failure, creep remains externally driven and self-stabilizing, whereas tertiary creep is governed by positive deformation–damage feedbacks that promote self-accelerating failure (Amitrano & Helmstetter, 2006; Main, 2000; Corcoran & Davies, 2018; Kemeny, 2003). This eventual transition to runaway acceleration, commonly termed a slow-to-fast transition, may coincide with peaks in external forcing, but can also occur weeks to months after forcing has subsided (Handwerger et al., 2019), or even in the absence of an identifiable external trigger (Lagarde et al., 2023; Schöpa et al., 2018a). Effective landslide early warning therefore depends on detecting the earliest onset of tertiary creep and distinguishing reversible transient accelerations, which may produce false alarms, from irreversible accelerations that progressively evolve toward catastrophic failure; failure to identify the latter in time can result in missed warnings (Intrieri et al., 2019). Two fundamental limitations complicate this problem. First, the temporal expression of pre-failure deformation spans a wide range of timescales, making it difficult to reliably distinguish the onset of tertiary creep within limited monitoring windows. External forcings can mask or modulate the system response, complicating the identification of signatures associated with internally driven destabilization. Second, internal damage evolution is not necessarily expressed at the surface, limiting the ability of surface-based observations to capture the underlying failure processes. Although geodetic and remote sensing techniques are effective for monitoring slow, progressive deformation, they may fail to resolve the terminal acceleration phase because of sparse temporal sampling and loss of signal coherence during rapid motion (Moretto et al., 2021; Manconi, 2021). In contrast, in situ

instruments are often destroyed or rendered inoperable as deformation accelerates toward failure.

With high temporal resolution and the ability to monitor entire slopes using sparse distributed sensor networks, seismic monitoring provides a non-invasive means to track evolving instability. (Poli, 2017b; Schöpa et al., 2018a; Yamada et al., 2016b; Amitrano & Helmstetter, 2006; Provost et al., 2018; Dietze et al., 2021a). When combined with machine-learning approaches, even weak and intermittent precursory signals embedded in noise can be systematically detected and tracked, extending observational access to the internal evolution of landslides across both quiescent and rapidly accelerating phases (e.g., Seydoux et al., 2020; Provost et al., 2017b). Here, we analyze continuous seismic data from a local sensor network to investigate the slow-to-fast sliding transition of the 2023 Brienz/Brinzauls rockslide in the eastern Swiss Alps (2×10^6 $\mathbf{m^3}$). This event provides a rare opportunity to examine the internal processes that drive a large slope failures: both the runaway acceleration and the final collapse occurred under dry conditions, above-freezing temperatures, providing an opportunity to examine the characteristics of internal processes in isolation of meteorological influences. Using a supervised machine-learning model, we track the spatiotemporal evolution of subsurface cracks and surface rockfalls originating from the moving mass throughout the transition. By integrating seismic observations with surface kinematic measurements, we address three guiding questions: (1) how did the relative influence of external forcing and internal processes evolve over time? (2) how did the basal slip interface and the mobilized mass co-evolve? and (3) which observable markers signaled the onset of runaway acceleration? We find that the rockslide progressively transitioned from externally forced, rainfall-driven deformation to internally driven instability approximately 37 days before collapse, marking the onset of runaway acceleration that ultimately culminated in catastrophic failure.

2 Study site and the June 15, 2023 rock-slope failure at Brienz/Brinzauls

The 15 June 2023 rockslide that threatened the village of Brienz/Brinzauls (hereafter Brienz) occurred within a large Holocene deep-seated gravitational slope deformation (DSGSD) in eastern Switzerland. Extending from Piz Linard (2,767 m a.s.l.) to the Albula River (∼900 m a.s.l.), this instability poses a substantial risk to critical infrastructure—including cantonal roads, a railway corridor with UNESCO World Heritage status, and transnational energy and communication lines—and has therefore been the focus of intensive long-term monitoring and mitigation efforts, accompanied by elevated public and scientific attention.

The most dynamic part of the complex comprises two mechanically coupled domains (Fig. 1A). The lower domain (∼1–2 $\times$ 10^8 m^3) hosting the village of Brienz is largely cultivated and forms a slowly creeping, undulating mass composed of Flysch (∼1.5 $\times$ 1.3 km in extent, ∼250 m of relief) bounded by a well-defined basal sliding surface (Figi et al., n.d.) between the Albula River to the south and sharp lateral boundaries to the east and west. The upper domain (∼1–2.5 $\times$ 10^7 m^3), located directly upslope of the village, consists of dolomites, rauhwackes, and marly schists (Krähenbühl & Nänni, 2017). In the two years preceding the collapse, a discrete kinematic unit—later termed the Insel section (Island)—developed within the upper domain as a mechanically independent block (Fig. 1B), bounded by a fully formed basal rupture surface and well-defined lateral margins. During our analysis period, total-station measurements showed little variation in reflector plunge, indicating that deformation was primarily accommodated by sliding along a well-developed rupture surface rather than by progressive toppling (Loew et al., 2025a). The same study also revealed strong geometric and lithological heterogeneity within the unstable mass. The basal failure plane was steep beneath the upper Insel (∼45°) but progressively flattened to ∼20° beneath the lower Insel, while fractured Vallatscha dolomite in the upper Insel transitioned downslope into weaker schistose units in the lower Insel (Fig. 1B). Together, this bilinear basal geometry and contrasting lithol-

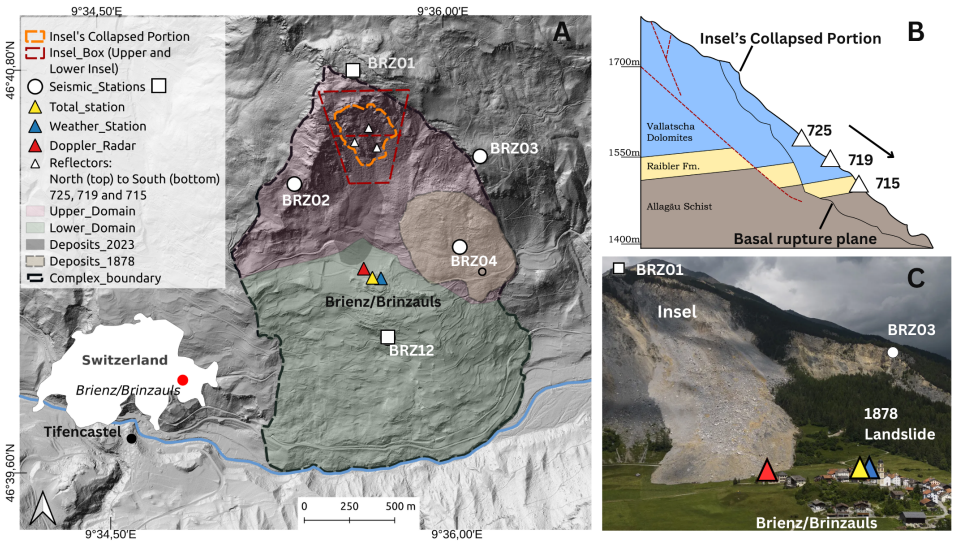

Figure 1: **Overview of the Brienz/Brinzauls deep-seated gravitational slope deformation (DSGSD) and the 2023 rockslide source area.** (a) Map showing the interconnected domains of the DSGSD complex and the source area of the June 2023 rockslide within the *Insel* sub-volume, together with surrounding seismic stations (TC120s shown as squares and PE6Bs as circles), a weather station, and Doppler radar directed toward the *Insel*. (b) Schematic cross-section of the failed *Insel* compartment illustrating the compound nature of the slide, with an active, brittle domain in Vallatscha dolomites overlying a passive wedge in weak Allgäu schists. Bedding in the Vallatscha Formation dips steeply out of the slope, while that in the Raibler and Allgäu Formations dips gently into the slope. The schematic cross-section is adapted from Loew et al. (2025b). (c) Landslide above Brienz/Brinzauls, Switzerland, viewed north–northeast, showing recent debris runout that nearly reached the village. Image credit: Michael Buholzer/Keystone

ogy led to the instability being classified as a compound rockslide (Hungr et al., 2014; Loew et al., 2025a). Following the development of a basal rupture surface, the Insel subvolume underwent a prolonged ∼4-month phase of accelerating deformation before collapsing during the night of 15 June 2023. Failure initiated with multiple detachments at the toe of the Insel that generated dry granular flows, followed by one or more major collapse events Loew et al. (2025a). The main failure registered on regional seismic stations at 21:38 UTC. The runout stopped just short of the village (Fig. 1C). Debris slides and secondary rockfalls continued for several hours afterwards. Because the failure occurred at night, optical and daylight-dependent monitoring systems did not capture the full sequence, and the exact timing and volumes of the sub-events remained only partially constrained.

For early warning, the Voight–Fukuzono approach (Voight, 1988a; Fukuzono, 1985a) was applied by the authorities Loew et al. (2025a), with alert thresholds based on expected velocities at predefined lead times (Crosta & Agliardi, 2003a). However, deviations from classical creep behavior undermined the reliability of the forecasts. As deformation accelerated, authorities issued an evacuation instruction on 5 May 2023. The final abrupt acceleration on 15 June 2023 was not anticipated by any predictive model. The collapse has since been examined from multiple perspectives (Loew et al., 2025a; Kenner et al., 2025; Kang et al., 2024b; Borgeat et al., 2024; Manconi et al., 2024).

3 Materials and Methods

To monitor vibrations generated by internal deformation of the Insel compartment and mass movements at its surface, we deployed a small network of seismic stations consisting of three three-component geophones (PE-6/B) and two broadband seismometers (Trillium Compact 120 s) (Fig. 1a), all recording at 100 Hz using DIGOS DataCube3ext loggers. The seismic stations had operated intermittently since October 2020; our analysis focuses on a 57-day interval between 21 April and 17 June 2023. 11 Within this interval, we analyze data from three stations (BRZ02, BRZ03, and BRZ04) situated in the upper domain, surrounding the deforming Insel rock mass. To complement the seismic observations, We use previously published surface kinematic and meteorological data presented by Loew (2024), including total-station reflector measurements from the Insel (Fig. 1B) and observations from the Brienz weather station.

We approach the analysis of internal slope processes as a seismic event detection and classification problem. Because no predefined event catalog exists, we first construct an initial event pool by scanning the continuous seismic record for discrete amplitude transients using a short-term average–long-term average (STA–LTA) detector and clustering the resulting waveforms by similarity to identify families of repeating sources (refer to Supplementary Information, Section 1.1, for methodological details). These events are subsequently located (refer to Supplementary Information, Section 1.1.1) and compared with detections from a Doppler radar catalog (Geopraevent, 2022), which records only surface mass movements, allowing subsurface seismicity to be distinguished from processes at surface. We define and curate four seismic classes—surface events, sub-surface events, tectonic earthquakes, and background noise. Building on this initial classification, we perform a second analysis using a supervised machine-learning detector trained on manually curated examples to identify and classify seismic signatures associated with distinct physical processes, thereby enabling the construction of a more complete event catalog. Details of the approach are provided below.

3.1 Construction of Training Labels for Supervised Learning

Surface Events: These correspond to surficial mass movements such as rockfalls, involving the detachment and downslope movement of rock fragments through sliding, rolling, or free fall. Rockfalls (Fig. 2A) generate long-duration (more than 5 sec), emergent seismic signals composed of multiple short, high-frequency transients (1–45 Hz) due to successive impacts and inter-particle collisions (Burtin et al., 2016a; Helmstetter & Garambois, 2010; Lacroix & Helmstetter, 2011). In addition, we use a catalog of rockfalls detected by the Doppler radar, which provides independent constraints on the timing of downslope debris movement. Spectrograms of radar detections are visually inspected to confirm corresponding seismic signatures, yielding 11 287 labeled surface events for training (16 May–14 June) and 96 for testing (15–29 June). While not treated as absolute ground truth, the radar detections provide a robust and independent basis for surface-event labeling.

Sub-surface Events: Prior near-field studies associate short-duration (< 5 s), high-frequency ($\sim$1–20 Hz), impulsive microseismicity with crack growth and shear failure within a deforming mass (e.g., Helmstetter & Garambois, 2010; Lacroix & Helmstetter, 2011; Dietze et al., 2021b; Provost et al., 2017a). These signals (Fig 2B) show sharp onsets, rapid amplitude decay, and often appear on only a subset of stations due to attenuation. We manually review STA–LTA detections and retain 11 322 events from within the Insel and 295 from surrounding slopes, together with 100 manually identified events missed by the STA–LTA detector, yielding 717 labeled sub-surface events for BRZ02. Owing to the coherent recording of these events across nearby stations, the same catalog is applied to BRZ03. In contrast, BRZ04 is situated on deposits of the 1878 Igl Rutsch landslide, where strong attenuation degrades waveform quality; consequently, this sta-

tion is treated separately, and only 79 events from the original catalog are retained as clear sub-surface signals for training.

Tectonic Earthquakes: The Alps are seismically active. Therefore, we define a separate class for local and regional earthquakes. These events exhibit impulsive onsets with identifiable P– and S-phases and triangular spectrograms with high-frequency onset tapering to lower frequencies due to dispersion and scattering (Figure 2c). We first use regional earthquake detections from the Swiss Seismological Service (Graubünden region), and additionally query the IRIS FDSN service (Incorporated Research Institutions for Seismology (IRIS), 2023) for cataloged events within 10° of the LIENZ station (400 km away). By inspecting both catalogs and corresponding spectrograms, we match origin times to observations in the local Brienz network. This yields 78 labeled earthquakes at BRZ02, 16 of which are recorded across all three field stations during the core observation window (21 April–30 June 2023).

Background Noise: Noise includes both quiescent periods (Figure 2d) and transient non-slope signals such as rainfall-induced broadband bursts and narrow band tonal energy linked to air and ground traffic and other anthropogenic sources. The final noise catalog consists of 175 manually selected windows (10–600 s) from 21 April–30 June 2023, supplemented by 149 additional windows from January 2023 (only BRZ02 operational), ensuring representation of low-activity periods.

3.2 Supervised Classifier Training and Deployment on Continuous Seismic Data

3.2.1 Model Training and Testing

To classify seismic signals in continuous recordings, we train separate supervised multi-class XGBoost models (v2.1.4) for each station (BRZ02, BRZ03, and BRZ04) using manually labeled data. The objective is to learn discriminative mappings from a set of statistical features to the previously defined four seismic source classes. XGBoost, an ensemble tree-based method, enables effective class separation while limiting overfitting (Chen & Guestrin, 2016) and shows robust performance and generalization across sites and seismic event types in recent monitoring studies (Zhou et al., 2025; T. Wang et al., 2023).

We extract 92 statistical features from the labeled events using a 2 s sliding window applied between the manually annotated start and end times. We use a 50% window overlap for all classes, except for sub-surface events where a higher 90% overlap is adopted to augment the comparatively limited training data and improve generalization, albeit at the cost of increased sample redundancy. Manual labeling indicates that sub-surface events typically last ∼0.5–5 s, whereas regional/teleseismic earthquakes and surface mass-movement signals (e.g., rockfalls and debris mobilizations) generally exceed 5 s. The 2 s analysis window therefore provides a practical compromise: it is short enough to capture transient sub-surface signals while remaining sufficiently long to preserve the characteristic waveform structure of longer-duration sources. We compute features from the 1–49 Hz band, spanning time- and frequency-domain descriptors, including waveform-shape metrics (e.g., rise/fall time, skewness, peak-to-mean ratios) and frequency-domain properties (e.g., number of peaks in the power spectrum, mean and variance of spectral power), providing a robust representation of event sources (see Supplementary Table 2 for a complete feature list).

The labeled dataset, now composed of 2 s analysis windows, is randomly split into 80% training and 20% testing subsets while preserving class proportions. Owing to inherent class imbalance and station-specific detection rates, the number of samples per class varies between stations (see Supplementary Material 1.2 for details on training and testing set sizes). To evaluate model performance and generalization capability, we ap-

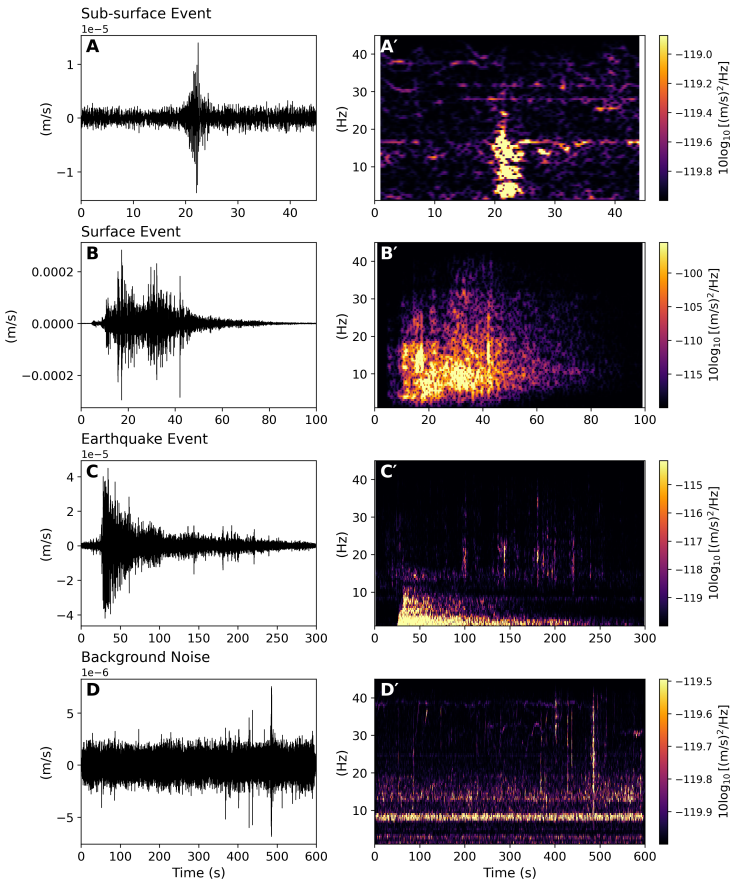

Figure 2: **Representative examples of seismic event classes and labeling scheme.** Panels (a–d) show characteristic waveform and spectrogram signatures for the four categories used in this study: (a) surface events associated with rockfalls and mass movements, (b) subsurface (crack-like) events originating within the rockslide source area, (c) tectonic earthquakes displaying impulsive body-wave phases, and (d) background noise encompassing environmental and anthropogenic signals. These examples illustrate the features used to construct the labeled catalog for machine-learning analysis.

ply 5-fold cross-validation independently at each station. This approach tests the model's sensitivity to any single train–test split, helps ensure that it learns general patterns rather than station-specific noise, and provides more reliable performance estimates across varying data subsets (e.g.(Markatou et al., n.d.)). We quantify model accuracy using standard classification metrics, with particular emphasis on the F_1 score—a balanced measure of precision and recall that is well suited for imbalanced datasets (Siblini et al., 2020). To further increase confidence, we combine predictions from the three station-specific models in an ensemble framework and evaluate performance at network level. Ensemble voting requires a minimum classification confidence of 0.7 and agreement from at least two models across all classes. For earthquake detections, however, we give precedence to classifications from BRZ02 over the ensemble outcome due to its consistently higher performance and larger earthquake training set. Details of the ensemble voting evaluation, including the construction of the shared test dataset and the individual and network-level confusion matrices, are provided in the Supplementary Materials 2.1.

3.2.2 Machine Learning Classification of Events in Continuous Seismic Data

We applied the trained models to continuous seismic data from 21 April to 17 June 2023 across all three stations to identify weak events missed by conventional STA–LTA detection and manual inspection. For each station, the same set of features was extracted using a 2-second sliding window with 50% overlap. Thus, each time step of the incoming continuous data stream is assigned to a specific event class with associated output probabilities; classifications of surface and subsurface events are retained only when the predicted class probability exceeds 0.7 at at-least two stations. Since rockfalls (Surface events) typically span durations longer than the 2-second sliding window, consecutive windows with identical classifications are aggregated to form single continous events. To minimize double counting during downslope propagation, detections occurring within 15 s of a preceding rockfall/avalanche signal were merged and treated as a single event. This approach reduces the likelihood of repeatedly counting the same mobilized rockfall or avalanche mass as it propagates downslope and generates multiple seismic detections. The selected 15 s merging window represents a conservative first-order transport timescale, justified by the site geometry, including an average slope inclination of 28°, a vertical relief of 538 m, and an estimated along-slope travel distance of 850–1000 m. These topographic conditions permit rapid downslope motion on timescales of several tens of seconds. Importantly, the adopted 15 s threshold remains substantially shorter than the minimum inter-event separation of 58 s observed in the independently validated Doppler-radar rockfall catalogue, thereby minimizing the risk of incorrectly merging distinct physical events. Each subsurface event is short-lived and may be represented by only one or two windows. As a result, their detection is more susceptible to undercounting when small travel-time differences occur between stations. Given a maximum inter-station distance of 1000 m within our network, we apply a temporal buffer equal to the expected propagation time across the array (inter-station distance divided by the assumed seismic velocity of 500 m s^{-1}). This ensures that detections originating from the same event are not treated as separate triggers simply because of modest travel-time offsets. Event locations were determined following the methodology described in SI 1.1.1 . For long-duration surface events, only the initial 10 s of signal were used to locate the onset of activity, rather than the subsequent downslope transport. Events with durations outside their expected ranges—subsurface events longer than 5 s and surface events shorter than 5 s—were excluded from the final analysis catalog.

3.3 Analyzing the Machine Learning Derived Event Catalog

To separately analyze subsurface and surface seismicity, we first impose physically meaningful spatial constraints. We define a polygon outlining the rockslide source region (the Insel) and subdivide it into upper and lower sectors (Figure 1a). This partition reflects the lithological zonation within the Insel, separating the schistose lower Insel from the dolomitic upper Insel (Loew et al., 2025c).

3.3.1 Time-Resolved Growth Exponent

To investigate the temporal evolution of seismic activity, we compute the cumulative number of events, $\Omega(t)$, from the machine-learning–detected event catalog. Local finite-time growth behavior is then estimated using sliding windows containing 300 events and shifted by 50 events. Within each window, a power-law relationship is fitted to $\Omega(t)$ to derive a time-dependent growth exponent (see SI 2.1), $\alpha(t)$. This procedure is applied independently to surface and subsurface seismicity, yielding $\alpha_{\mathrm{surf}}(t)$ and $\alpha_{\mathrm{sub}}(t)$, respectively. Their ratio,

$$R_{\text{surf-sub}}(t) = \frac{\alpha_{\mathrm{surf}}(t)}{\alpha_{\mathrm{sub}}(t)},$$

provides a quantitative measure of the relative dominance of surface and subsurface processes.

3.3.2 Change Point Detection

To identify statistically significant transitions in growth behavior, we apply a Bayesian Information Criterion (BIC)–optimized binary segmentation independently to the $\alpha_{\text{surf}}(t)$, $\alpha_{\text{sub}}(t)$, and $R_{\text{surf-sub}}(t)$ time series. This approach identifies change points while penalizing over-segmentation and reducing sensitivity to noise-driven fluctuations. Further methodological details are provided in the Supplementary Material section 1.5.

3.3.3 Correlation with bulk kinetics

To investigate the relationship between seismic activity and surface kinematics, we analyze surface velocity measurements derived from three total-station reflectors (IDs 715, 719, and 725) that remained continuously operational throughout the study period. Two-hourly displacement measurements are first averaged to daily mean velocities for each reflector. These daily velocities are then averaged across the three reflectors to obtain a single Insel-wide daily surface velocity time series, $v(t)$. In parallel, seismic detections are aggregated into daily-binned event counts. Temporal co-variation between daily surface velocity and seismicity is first assessed using the Spearman rank correlation coefficient (ρ), computed in logarithmic space. While Spearman correlation captures monotonic relationships, it does not quantify proportional scaling between deformation and seismic release. To address this, we further examine the evolving relationship between seismic activity and Insel slip by evaluating the cumulative event–cumulative velocity ratio,

$$R_{\text{event-slip}}(t) = \frac{N(t)}{\Omega(t)}, \tag{1}$$

where $N(t)$ denotes the cumulative number of detected seismic events and $\Omega(t)$ is the cumulative surface slip obtained by integrating the daily velocity time series $v(t)$, with $v(t) = \frac{d\Omega}{dt}$. The ratio $R_{\text{event-slip}}(t)$ thus quantifies the number of microseismic events produced per unit of slip and provides a proxy for the evolving seismic efficiency of deformation. The corresponding event rate is given by $\frac{dN}{dt}$. The same analysis is repeated considering only surface seismic events.

3.3.4 Correlation with meteorological drivers

Rainfall episodes (P1–P5; Figure 4b) were identified from cumulative rainfall trends and resolved into sub-events exceeding 0.2 mm h^{-1}. Sub-events separated by less than 4 h were merged into single storms to quantify rainfall duration, accumulation, intensity, and sub-spell structure. To evaluate its influence, we integrate precipitation, surface displacement, and seismic detections at high temporal resolution, derive daily surface acceleration, and apply prominence analysis (see Supplementary Material) to the event–slip ratio $R_{\text{event-slip}}(t)$ to quantify transient increases in seismic productivity relative to the local background. Finally, Thermal influences are assessed through Spearman rank correlation between hourly temperature changes and seismic event rates.

4 Results

4.1 Spatial Distribution of Seismic Sources

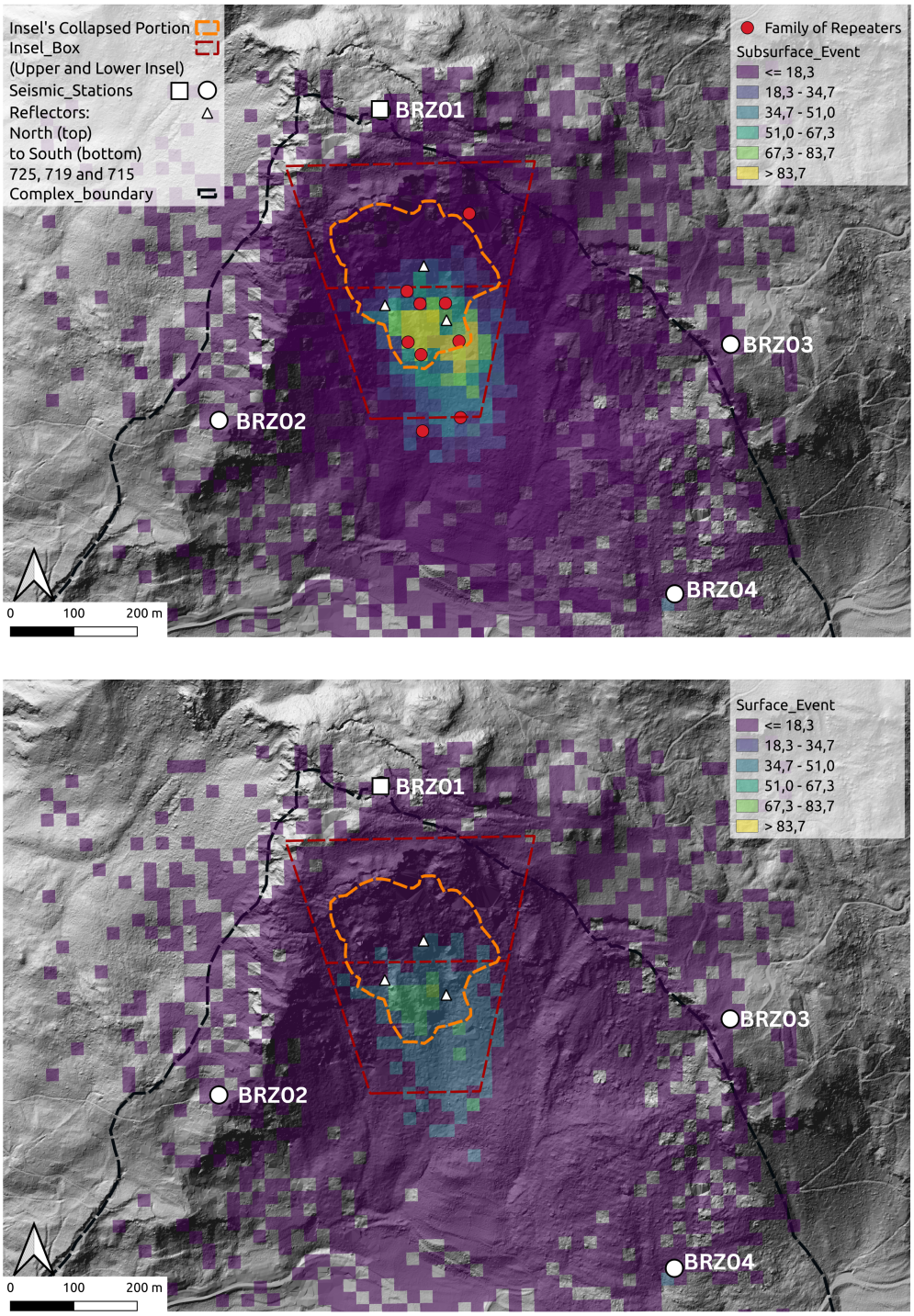

Figure 3: Spatial distribution of seismic sources. (**a**) Corresponding sub-surface detections, including families of repeating events. (**b** Locations of all detected surface events. White triangles mark total-station reflectors; from north (top) to south (bottom) these are 725, 719, and 715. Only events within the Insel polygon are retained for subsequent analyses. The orange boundary delineates the mapped source area of the rockslide, adopted from Leow et al. (2025).

During the 59 days long study period, we detect 3,624 surface events and 6,152 subsurface events originating within the rockslide source area (the Insel polygon). Seismic activity exhibits a pronounced spatial asymmetry across the Insel. Surface seismicity is preferentially localized in the lower Insel, where 69.51% of events occur, compared to 30.49% in the upper sector (Fig. 3A). Accounting for the difference in areal extent—the upper sector being 1.57 times larger—the lower Insel exhibits a ∼3.58-fold higher surface-event density (events per unit area). This spatial contrast is even more pronounced for subsurface seismicity. A total of 85.32% of subsurface events originate in the lower sector, with only 14.68% occurring in the upper Insel (Fig. 3B), corresponding to a ∼9.13-fold higher subsurface-event density in the lower sector after area normalization. In addition, surface events extend downslope beyond the source area, delineating the talus slope as an active transit zone where detached material was transported, deposited, and intermittently re-mobilized. Despite lower surface gradients on the lower Insel schist compared to the upper Insel, rockfall source locations are 3.58× more frequent in the lower Insel (Fig. 3B). Notably, despite the generally lower surface gradients of the lower Insel schist compared to the upper Insel, rockfall source locations remain strongly concentrated in the lower Insel, spatially coinciding with intense sub-surface seismicity and repeating seismic families.

4.2 Temporal evolution of seismic sources

The system initially exhibits quasi-linear co-evolution of surface and subsurface activity, with short-lived bursts triggered by rainfall. Over time, this relationship diminishes as subsurface activity accelerates more rapidly than surface activity. Both signals then transition into a strongly non-linear, accelerating regime that culminates in the collapse. To resolve this progression, we subdivide the run-up phase into three successive intervals, labeled 1, 2, and 3 (Fig 4). Interval 1 (21 April–12 May 2023) corresponds to a wet phase comprising four distinct rainfall episodes (P1–P4), Interval 2 (13 May–26 May 2023) represents a comparatively dry phase with a single rainfall episode (P5), and Interval 3 (27 May–15 June 2023) is entirely dry and contains no rainfall events.

Figure 4B shows the temporal evolution of the surface (α_{surf}) and subsurface (α_{sub}) growth exponents through the three deformation intervals. During Interval 1, both surface (α_{surf}) and subsurface (α_{sub}) growth exponents remained mostly in a sub-linear to near-linear regime, with transient excursions during rainfall episodes. Superimposed on the baseline, rainfall episode P1 (23–25 April) produced short-lived spikes in surface and subsurface activity visible in the daily event bar plots, whereas P2 (30 April–2 May) is marked by growth exponents of seismic activity increasing to $\alpha_{\mathrm{surf}} \approx 1.83$ and $\alpha_{\mathrm{sub}} \approx 1.68$ before relaxing back to baseline values (≈ 0.75–0.85) by 3–4 May. Episode P3 (6–8 May) shows no significant excursion in either series. In contrast, P4 (9–12 May) elicits a distinctly asymmetric response, with α_{sub} increasing to ~ 1.31–1.34 and α_{surf} rising more modestly to ~ 0.95–1.20. Entering Interval 2, which marks the onset of a dry phase, the ratio $\alpha_{\mathrm{surf}}/\alpha_{\mathrm{sub}}$ progressively decreases, reaching a minimum of ~ 0.52 on 19 May, indicating sustained subsurface acceleration without a corresponding surface response. Thereafter, the ratio gradually increased toward unity as surface activity intensified, while the isolated rainfall episode P5 (24–25 May) produced no discernible effect on either of the individual growth exponents. During Interval 3, both surface and subsurface growth exponents increased markedly toward collapse. At the beginning of the interval, subsurface activity was slightly stronger, with $\alpha_{\mathrm{sub}} \sim 1.4$–$2.4$ compared to $\alpha_{\mathrm{surf}} \sim 1.4$–$1.8$. A pronounced but short-lived increase occurred around 31 May–1 June, when α_{sub} rose to ~ 3.6–4.0 and α_{surf} to ~ 2.3–2.9, followed by a decline in both exponents, with subsurface activity remaining dominant. The first breakpoint identified by Bayesian Information Criterion (BIC) segmentation occurs in the surface series on 12 June, where α_{surf} sharply increases from 1.62 to 5.44 (+235%), approximately three days prior to collapse. A subsequent breakpoint in the subsurface series is detected on 12 June, with α_{sub} rising from 2.07 to 5.61 (+171%). Despite subsurface acceleration, surface activity be-

comes increasingly dominant in the final day before collapse, as reflected by the ratio $\alpha_{\mathrm{surf}}/\alpha_{\mathrm{sub}}$ increasing from values below unity to ~ 2.4 by 15 June.

At 21:14 UTC on 15 June, the Insel entered the collapse phase, after which seismic records were dominated by high-amplitude signals characteristic of dry granular flow, indicating rapid release of fragmented material (Fig. 5). Rather than a single rupture, mass mobilization unfolded over approximately 24 minutes as a sequence of overlapping debris pulses, causing near-field signal saturation and preventing identification of individual events. The terminal pulse (21:38–21:39 UTC) was instead resolved by low-frequency (0.01–0.08 Hz) seismic waves recorded at station BRZ12, which capture both the acceleration and subsequent deceleration of the descending mass.

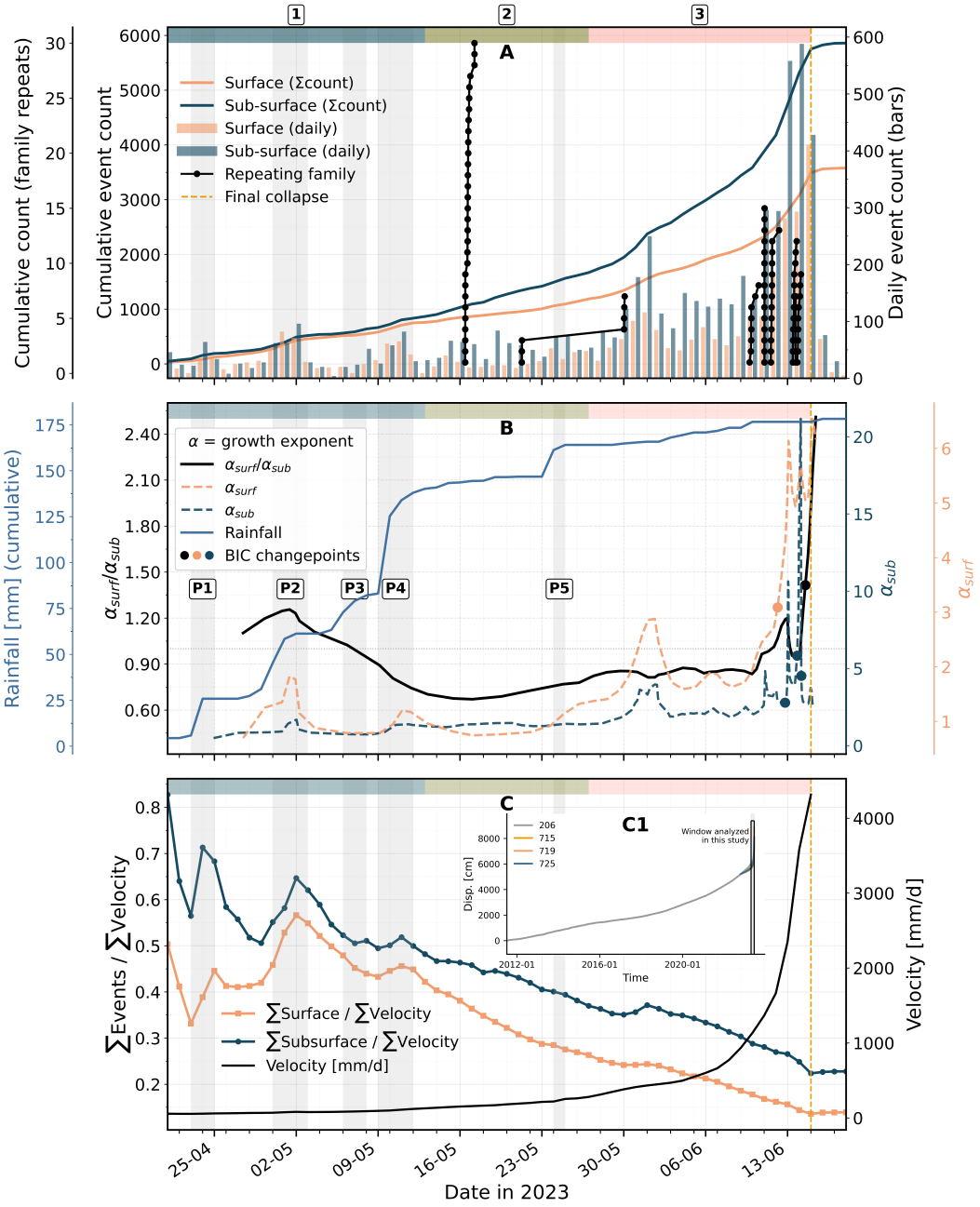

Figure 4: **Temporal evolution of seismicity, slope kinematics, and rainfall during the tertiary creep phase.** (a) Cumulative counts of surface and subsurface seismic detections, together with repeating sub-surface families and daily detection rates. Colored header bands define Intervals 1–3, highlighting successive phases of activity evolution. (b) Time-dependent local growth exponents $\alpha_{\mathrm{surf}}(t)$ and $\alpha_{\mathrm{sub}}(t)$, their smoothed ratio $\alpha_{\mathrm{surf}}/\alpha_{\mathrm{sub}}$, and BIC-selected changepoints identifying statistically distinct scaling regimes. Cumulative precipitation and rainfall episodes P1–P5 provide hydrometeorological context. (c) Evolution of seismic productivity relative to displacement, expressed as $\sum$Events/ $\sum$Velocity ratios, together with the combined surface velocity. The inset shows the long-term displacement evolution of key reflectors. The red dashed line marks the 15 June 2023 collapse.

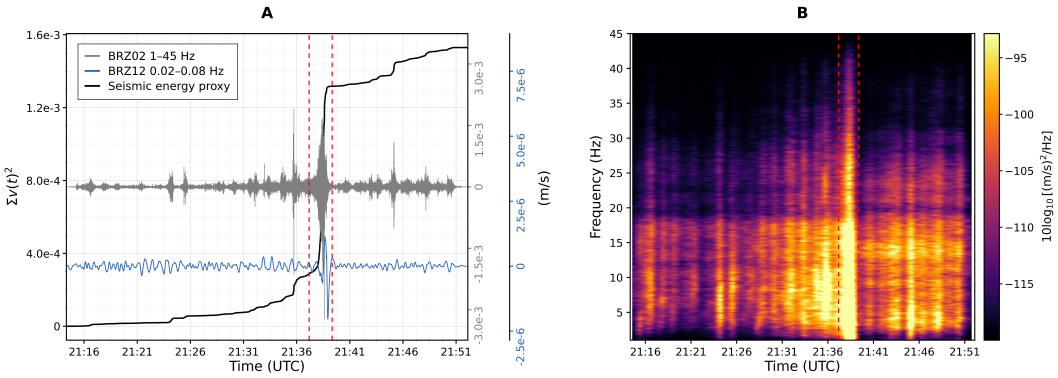

Figure 5: Final collapse sequence. (a) Waveform recorded at station BRZ02 (bandpass 1–45 Hz) overlaid with 60 s sliding-window cumulative seismic energy. The low-frequency vertical component (0.02–0.08 Hz) from the broadband station BRZ12 is superimposed for comparison. (b) Unfiltered spectrogram for the same time interval, illustrating the broadband energy release accompanying the terminal collapse.

4.3 Families of Repeating events

Within the pool of STA/LTA–detected transients, we identify eight repeater families using a waveform cross-correlation threshold of CC ≥ 0.8 (Fig. 6). The figure shows the temporal occurrence of all families along with representative waveform examples, while the complete set of waveforms is provided in the Supplementary Material. These families comprise 101 subsurface events, representing approximately 1.6% of all machine-learning–detected subsurface seismicity, indicating that the vast majority of events do not recur with sufficiently similar waveforms to form repeating families. Repeater activity is episodic and short-lived, with families appearing and disappearing prior to collapse rather than persisting throughout the deformation history. No repeater families are detected during Interval 1. The first repeater family (Family 1) emerges shortly after the onset of Interval 2, initiating on 16 May. This family repeats 30 times over approximately 19 h. Family 2, which persists for roughly 9 days with seven occurrences, marking the only repeater activity sustained beyond a single day. All remaining repeater families (Families 3–8) are confined to Interval 3, during the final phase of runaway acceleration preceding collapse. Between 7 and 12 June, velocity increased from ∼20 to >220 mm day^{-1}, coinciding with the rapid initiation and termination of Families 3–5. This was followed by an additional ∼4-fold increase in velocity to ∼950 mm day^{-1} between 12 and 14 June, during which Families 6–8 emerged sequentially near peak acceleration.

Spatially, six repeater families are concentrated in the lower Insel (fig 3a), where they are co-located with regions of dense subsurface seismicity identified by the machine-learning detector. Two additional families occur downslope along the margin of the source zone, and one family is located in the upper Insel. This distribution mirrors the broader spatial pattern of subsurface seismic activity, with repeater families preferentially emerging in lower Insel.

4.4 Relationship Between Surface Motion and Seismic Sources

Over the full observation period, surface velocity increased from approximately 4 cm day^{-1} to more than 500 cm day^{-1} prior to collapse. Surface velocity and subsurface seismicity exhibit a strong monotonic relationship in double-logarithmic space (Spearman $\rho \approx 0.83$; Fig. 7), indicating systematic co-evolution over the duration of observation. During the early phase, subsurface event counts display substantial scatter for a given ve-

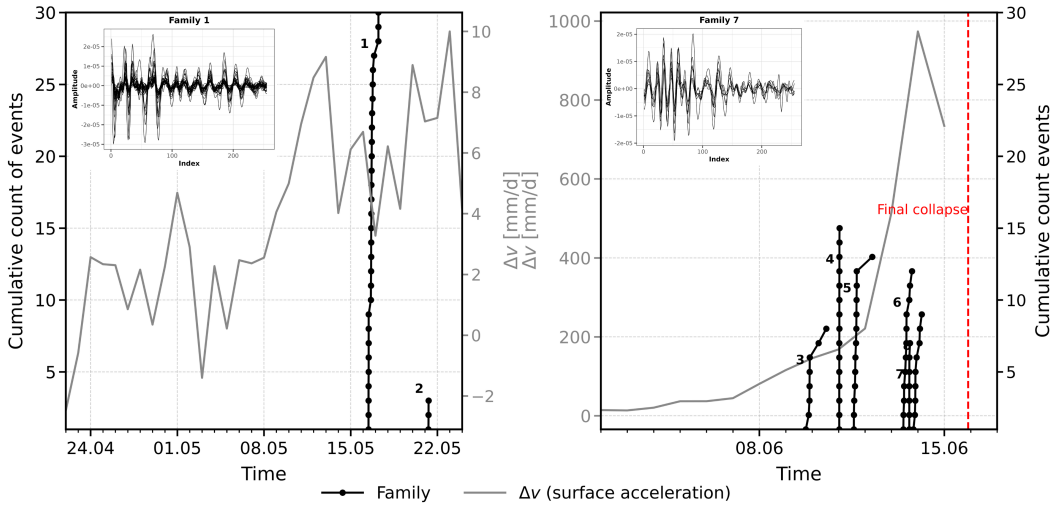

Figure 6: Repeating-family activity compared with surface acceleration. Black curves show the cumulative number of detections within two representative repeating families (Family 1 and Family 7) as a function of time. The grey curve shows the contemporaneous surface acceleration Δv (first temporal derivative of surface velocity), computed from the displacement time series of reflector 715. The red dashed line marks the final collapse. Insets show representative aligned waveforms from each family, illustrating their high waveform similarity. Waveforms from all identified repeating families are provided in Supplementary Material 2.6.

locity, reflecting the influence of rainfall episodes P1–P4. As conditions transition from wet to dry toward the end of Interval 1, this scatter progressively diminishes and the coupling between surface velocity and subsurface seismicity strengthens. When considered together, Intervals 1–2 show only moderate correlation ($r = 0.50$, $p = 0.002$). In contrast, Interval 3 is characterized by a tightly coupled regime with markedly reduced scatter and strong correlation ($r = 0.81$, $p < 0.001$)

Resolving the relative scaling between seismicity and slip, we find that during Interval 1 (Fig. 4c), both surface and subsurface event-to-velocity ratios ($\Sigma_{\mathrm{surf}}/\Sigma_v$ and $\Sigma_{\mathrm{sub}}/\Sigma_v$) exhibit pronounced but short-lived fluctuations that are closely associated with rainfall episodes P1–P4. Each rainfall pulse induces near-synchronous oscillations in both ratios, with local maxima during P1 (23–25 April) and P2 (30 April–2 May), followed by progressively weaker responses during P3–P4. These patterns indicate transient, externally forced increases in seismic productivity that rapidly relax once rainfall subsides, without leaving a sustained imprint on the longer-term slip–seismicity relationship. Interval 2 marks a clear and persistent shift in behaviour that continues through Interval 3 until final collapse. Across Intervals 2–3, both ratios decline steadily as surface velocity accelerates more rapidly than seismic event production. The sub-surface ratio decreased from $\sim$ 0.48 to $\sim$ 0.23 (a $\sim$ 53% reduction), while the surface ratio dropped from $\sim$ 0.42 to $\sim$ 0.14 (a $\sim$ 68% reduction). A brief transient around 31 May–1 June produced only a subtle inflection in both ratios, after which the long-term downward trend resumed. By 14–15 June, immediately prior to collapse, the ratios reached their minimum values of $\Sigma_{\mathrm{Sub}}/\Sigma_{\mathrm{v}} \approx 0.23$ and $\Sigma_{\mathrm{Sur}}/\Sigma_{\mathrm{v}} \approx 0.14$.

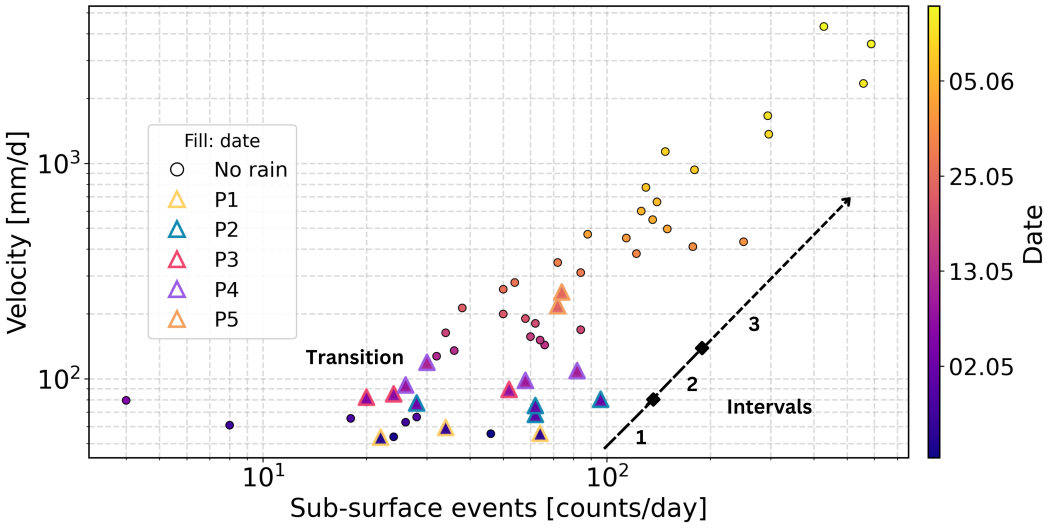

Figure 7: Log–log relationship between daily sub-surface event counts and daily mean velocity. Each point represents one day; circular markers correspond to days without significant rainfall, while colored triangular outlines highlight rainfall episodes P1–P5. The filled color denotes temporal progression from 21 April to 15 June 2023. A strong positive monotonic correlation is observed (Spearman $\rho \simeq 0.83$). Dashed arrows with interval labels (1–3) indicate selected temporal segments, provided to facilitate direct comparison with the corresponding intervals in the seismic event and velocity time series shown in Fig. 4.

4.5 Seismic Response to external forcing

During Interval 1, rainfall exerted a strong but evolving influence on the seismic response relative to slip. Episodes P1 and P2 produced delayed seismic responses following rainfall onset. During P1 (Fig. 8a; ~ 21.4 mm over ~ 8 h), both surface and subsurface seismicity increased within ~ 6 h of rainfall onset, with event rates peaking during the wettest period and decaying to background levels within ~ 24 h after rainfall cessation. Similarly, P2 (Fig. 8b), consisting of two rainfall pulses separated by a ~ 10 h dry interval, triggered a surface seismic response within ~ 1 h of rainfall onset, followed by sub-surface activity lagging by an additional ~ 1 h. Both responses decayed within ~ 28 h after the second pulse. Prominence analysis of the cumulative event–slip ratio isolates hydrologically driven amplifications by quantifying how strongly transient peaks rise above the local background, with higher values indicating enhanced seismic productivity relative to slip, while lower values grade into background behaviour, approaching zero in the absence of distinct peaks. The largest prominence occurs during P1 (surface $= 0.0569$; sub-surface $= 0.0797$; mean rainfall intensity ~ 2.65 mm h^{-1}), with comparably strong amplification during P2, for which the surface response is slightly stronger than during P1 (surface $= 0.0642$; sub-surface $= 0.0691$). In contrast, episode P3 (5–7 May; Fig. 8c), comprising two short rainfall bursts separated by ~ 22–24 h, produced no discernible increase in either surface or sub-surface seismicity and no resolvable prominence peak (surface $= -0.0025$; sub-surface $= 0.0036$).

Unlike for rainfall episodes P1 and P2, subsurface seismicity began accelerating on 8 May, approximately $\sim$48 h before the onset of the subsequent rainfall episode P4, without a corresponding increase in surface rockfall seismicity. Concurrently, reflector 715 in the southeastern sector of the Lower Insel exhibited an abrupt $\sim 4\times$ increase in surface acceleration; this is marked as a *transition* in (Fig. 6c). When P4 occurred (9–12 May;

∼51.8 mm over ∼32 h), it triggered an immediate spike in surface rockfall seismicity, whereas the subsurface event trajectory—already accelerating—showed no rainfall-related inflection. Consistent with this muted response, prominence values during P4 were moderate (surface = 0.0226; subsurface = 0.0254), approximately one-third of those observed during P1 and P2. By contrast, Interval 2 exhibits a near-complete loss of meteorological influence on seismicity. Episode P5 (Fig. 6d; $\sim$ 13 mm over $\sim$ 12 h) produced no measurable inflection in either surface or sub-surface seismic event rates and only minimal prominence (surface = 0.0035; sub-surface = 0.0064), despite brief, rapidly decaying acceleration spikes observed in surface reflectors.

Hourly temperature variations show only weak associations with seismic event-rate changes, with Spearman correlation coefficients remaining small ($|r| < 0.2$). This indicates that temperature fluctuations alone exert a limited influence on short-term seismic activity. The corresponding correlation plot is shown in Supplementary Fig.4.

5 Discussions

The commonly invoked "slow-to-fast" transitions observed in laboratory experiments and physical models have not yet been clearly resolved within the tertiary creep evolution of natural slopes, largely due to the historical lack of continuous seismic observations capable of capturing the internal deformation processes preceding failure. Previous studies primarily documented only the late stages of runaway acceleration, whereas the preceding and largely aseismic progression toward instability remained insufficiently constrained (Poli, 2017a; Schöpa et al., 2018b; Tiwari et al., 2022). Centered on the 8 May transition, we investigate how the evolving rate and state of internal deformation are encoded in the seismic catalogue, examine the changing conditions along the basal sliding surface and within the moving rock mass during and after the transition, place this transition within the broader evolution of tertiary creep, and discuss its implications for both early-warning forecasting and rockslide mechanics.

5.1 Linking Subsurface Seismicity to Internal Processes

The strong positive monotonic relationship between surface velocity and sub-surface seismicity (Spearman $\rho = 0.83$; Fig. 7) indicates that internal damage accumulation increased systematically as sliding velocities accelerated. As deformation rates increased, stress concentrations within the unstable rock mass promoted the initiation, propagation, and coalescence of fractures, generating transient seismic emissions associated with brittle cracking processes. The observed coupling between kinematic acceleration and seismic activity therefore suggests that sub-surface seismicity tracked the progressive degradation of the rock mass during the approach to failure (C. R. J. Kilburn & Petley, 2003; Brantut et al., 2013b; Dietze et al., 2021b; Weber et al., 2018). The abrupt disappearance of sub-surface events immediately after collapse suggest that these signals originated within the moving Insel mass or along its basal rupture interface, although their precise source depths remain unconstrained. Two end-member processes likely contributed to the observed seismicity: (1) stick–slip failure of interlocking asperities along the basal rupture surface during sliding (Brace & Byerlee, 1966; Finnegan et al., 2022; Yamada et al., 2016a; Aspaas et al., 2024; Poli, 2017a; Schöpa et al., 2018b), and (2) distributed internal damage within the deforming rock mass driven by stress concentrations and fracture growth away from the basal shear zone (Faillettaz et al., 2010a; Meng et al., 2024; Renard et al., 2020). Because these processes cannot be resolved independently, we interpret the sub-surface seismic catalogue as reflecting their combined contribution. This interpretation is supported by the nearly 9-fold increase in sub-surface seismicity and the clustering of repeating waveform families within the lower Insel (Fig. 3A). The underlying weak schist likely sustained increased loading as it buttressed the overlying competent dolomite, while the shallowly dipping rupture surface underneath provided rel-

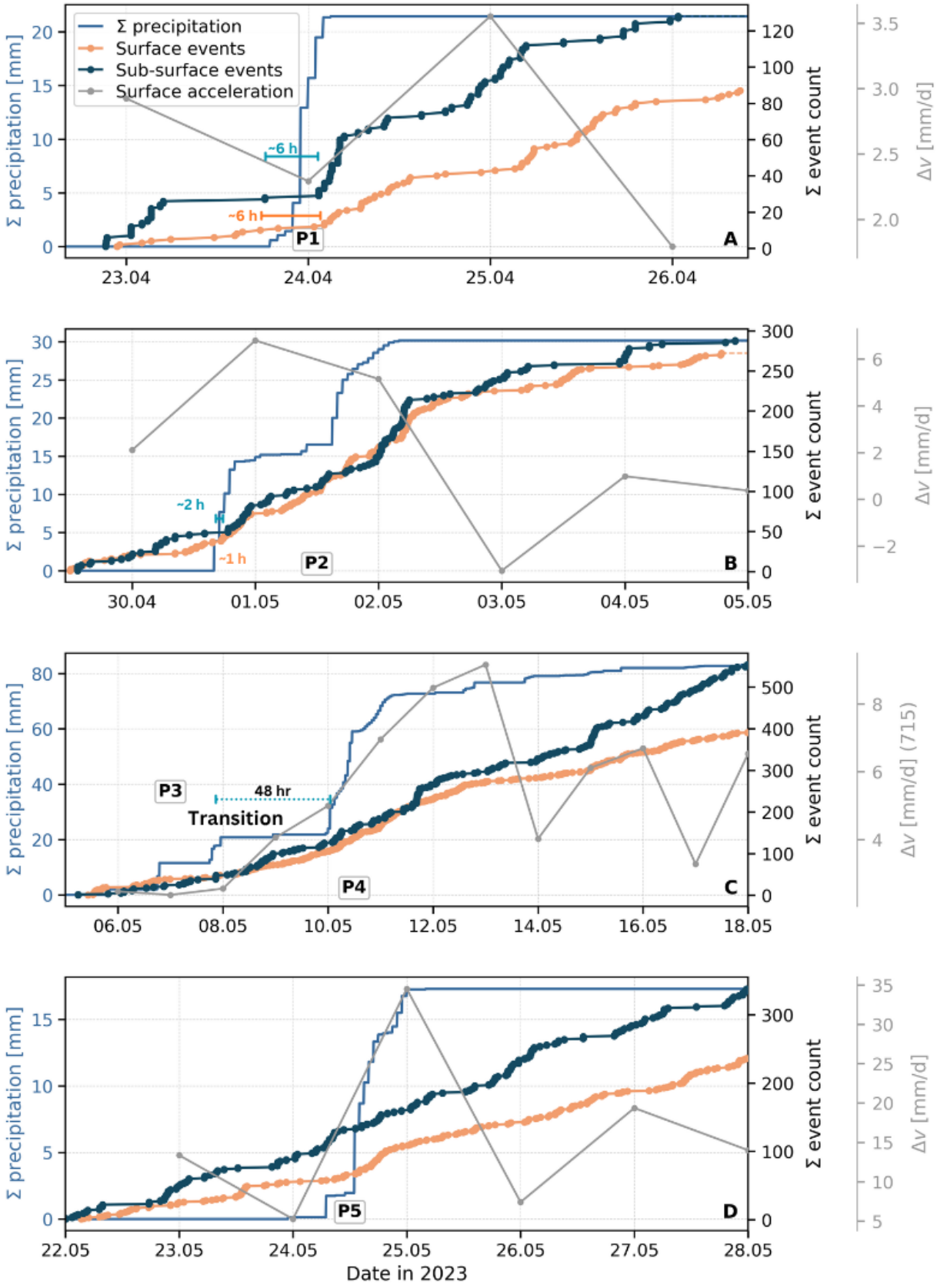

Figure 8: Each panel zooms into a single episode and compares cumulative precipitation (blue) with cumulative surface and sub-surface seismic event counts, together with daily surface acceleration (Δv, red). Panels correspond to (a) P1 (23–25 April 2023), (b) P2 (30 April–3 May 2023), (c) P3–P4 (6–12 May 2023), and (d) P5 (24–25 May 2023).

atively high resistance to sliding. Together, these conditions promoted stress accumulation, enhanced basal shearing, stick–slip failure, crack growth, and progressive internal fragmentation.

5.2 Transition: External control to Internal control

Rainfall can transiently enhance slope deformation by increasing pore pressure along the basal shear zone and by pressurizing pre-existing fractures, thereby promoting sliding and crack growth within the rock mass (Handwerger et al., 2013; Guglielmi et al., 2021; Dutler et al., 2020). Rainfall episodes P1 and P2 preceding the transition produced short-lived accelerations in both seismicity and bulk motion that rapidly decayed following rainfall cessation, indicating deformation sustained primarily by external hydrological forcing. Once the hydrological forcing was removed, both seismic activity and surface acceleration decreased, consistent with pore-pressure dissipation, recovery of effective normal stress, and a corresponding regain in basal frictional resistance, suggesting a largely reversible deformation response during this stage. This pattern changed across the 8 May transition. Sub-surface seismicity began accelerating nearly 48 hours before rainfall episode P4, exhibited only a relatively muted response during P4, and remained persistently elevated after rainfall ended. In contrast, following P4, surface rockfall activity declined while sub-surface seismicity continued to intensify under dry conditions until collapse. This decoupling from external hydrological forcing marks a transition from a rainfall-modulated regime characterized by cyclic acceleration–deceleration behaviour to an internally controlled regime dominated by progressive, seismically registered damage accumulation under gravitational loading. Further evidence for this shift to dominance of internal processes, is provided by the absence of any detectable response during the subsequent rainfall episode P5, despite comparable rainfall intensities. Surface kinematics clearly express this regime change. Mean reflector acceleration increased only modestly from 1.57 mm/d^2 before P1 to 1.79 mm/d^2 between P1 and P2, before declining to 0.97 mm/d^2 between P2 and P4 (Appendix Table 1). At P4, reflector 715 exhibited a nearly fourfold increase in acceleration (Fig. 8c), marking an abrupt departure from the preceding behavior. Importantly, this increase did not subside following the transition. Instead, mean reflector acceleration remained elevated at 7.23–8.79 mm/d^2 during the subsequent ∼10 days, approximately 7–9 times higher than during the P2–P4 interval, and continued to intensify thereafter toward collapse. Similar transitions have been observed in laboratory and theoretical studies, where frictional weakening, strain localization, and the breakdown of stabilizing feedbacks drive runaway acceleration (Handwerger et al., 2016b; Agliardi et al., 2020b; Paul et al., 2024a).

5.2.1 Progressive Conditioning of the Basal Surface as an Internal Driver

To identify a plausible mechanism governing the shift from externally forced slope deformation to internally driven acceleration, we synthesize the key concurrent observations following the transition: (1) a steady decrease in the ratio of sub-surface seismicity to slip, suggesting progressively more efficient sliding, whereby displacement accumulated faster than sub-surface seismicity. (Fig. 4C); (2) a similar decline in the ratio of cumulative surface events to slip (Fig. 4c); and (3) a divergence between surface and sub-surface seismicity, with surface activity progressively lagging behind the accelerating sub-surface trend (Fig. 4B). Comparison with daily mean RMS amplitudes at station BRZ02 — used as a proxy for evolving background noise levels — indicates that both sub-surface and surface event detections continue to increase relative to RMS after the transition despite progressively rising noise levels (Appendix Fig. A1).

Although the landslide volume likely comprised a continuum from coherent rock blocks to highly fragmented debris, rockfall activity declined relative to both sliding rates and sub-surface seismicity despite progressively faster motion. If deformation had become increasingly distributed throughout the landslide body, enhanced fracturing and

rockfall generation would be expected. Instead, the disproportionate increase in sub-surface seismicity and slip suggests that deformation became progressively localized within the basal shear zone. Such localization would promote the maturation of the basal slip surface through asperity wear, gouge production, and frictional weakening, allowing increasingly efficient slip accumulation prior to collapse (Guérin-Marthe et al., 2023; Goebel et al., 2024; Noël et al., 2023a). The available observations do not constrain the hydrological conditions within the shear zone, including potential water accumulation along the basal interface or whether the shear zone remained efficiently drained. Nevertheless, sliding became progressively more efficient and continued to accelerate toward collapse despite the absence of significant rainfall forcing, suggesting that the evolving basal shear zone had become a self-sustaining driver of instability through reduction of basal resistance. Interestingly, the onset of increasingly efficient sliding around 8 May coincided with the period when Loew et al. (2025c) reported that more than 50% of representative monitoring points exceeded the 15-day velocity threshold within the Voight acceleration framework, prompting evacuation recommendations for the village of Brienz. The seismically identified transition on 8 May coincides with the onset of strong acceleration at reflector 715, whereas reflectors 719 and 725 exhibit comparable acceleration only on 10 May, influenced by rainfall episode P4 (Appendix Fig. A1). This temporal offset suggests that the transition to runaway acceleration may have nucleated near reflector 715.

5.2.2 Origin of Repeaters

The small subset of subsurface events forming repeating families of nearly identical waveforms indicates stable source and propagation conditions (e.g., Nadeau & McEvilly, 1999), suggesting mechanically persistent asperities or localized stick–slip patches along the basal slip surface. Across all families, inter-event intervals do not systematically shorten toward failure but instead display pronounced irregularity and over-dispersion, with variances comparable to or exceeding the mean recurrence interval, while peak amplitudes within each family remain temporally erratic and show no monotonic trend. The transient nature of these repeating families, their irregular recurrence, and their preferential emergence during periods of rapid acceleration—including the appearance of the first repeater family following the ∼4-fold increase in surface acceleration and the subsequent occurrence of families 3–8 during the final runaway phase (Fig. 6a,b)—point to evolving asperity-scale mechanics. These may reflect intermittent engagement of freshly detached fragments with the shear layer or episodic reactivation of pre-existing sticky patches under variable stress conditions. However, their overall contribution remains limited, comprising only ∼1.6% of all subsurface events.

5.2.3 Response from the Sliding Mass

Surface seismic events reflect material detachment and downslope mobilization at the slope surface (e.g., Dietze et al., 2017; Schneider et al., 2023a) and are independently corroborated by Doppler radar observations (see Text S2.2 in the Supporting Information). As shown in Appendix Fig. A2, rockfall occurrence was not random but temporally clustered, as they show an excess of short waiting times and a heavier-tailed survival distribution relative to that expected for a Poisson process. Following the 8 May transition and the temporally overlapping P4 rainfall event, the surface-to-sub-surface seismicity ratio decreased by 20–25% during Interval 2, reflecting a relative decline in rockfall activity as sub-surface deformation and landslide acceleration continued to intensify.

The surface-to-sub-surface seismicity ratio began to rebound approximately 9 days after the transition, indicating a delayed increase in rockfall activity relative to sustained crack-related sub-surface seismicity. Because this rebound occurred in the absence of significant rainfall or temperature forcing, it likely reflects internal mechanical evolution of the landslide volume. This may have involved progressive stiffness degradation driven

by continued fracture growth and coalescence within intact rock, unjamming and mobilization of fragmented material, or both, ultimately increasing the susceptibility of material to detach and generate rockfalls. Progressive degradation of the mechanical stiffness of the landslide volume became most evident immediately prior to failure. A breakpoint in the surface seismicity series identified using Bayesian Information Criterion (BIC) segmentation on 11 June marked an abrupt increase in sur from 1.6 to 5.7 (+255%), approximately four days before collapse. This transition coincided with a 3–4-fold increase in the surface-to-subsurface seismicity ratio over the final three days, indicating enhanced near-surface fragmentation and rockfall activity. Consistent with the presence of a highly fragmented volume, cumulative seismic energy—used here as a proxy for transported volume (e.g., Hibert et al., 2014)—shows that the largest terminal pulse between 21:38 and 21:39 UTC accounted for only 78% of the total recorded energy (Fig. 5a). Thus, a substantial fraction of the mass was released progressively throughout the collapse sequence rather than during a single instantaneous failure. Such progressive fragmentation and disaggregation would also be expected to modify internal hydrological pathways, potentially explaining the reduction in seismic response lag from 6 h during P1 to 2 h during P2 despite lower rainfall intensities, and the absence of a detectable seismic response during P5 despite rainfall intensities comparable to or exceeding those of P2.

5.3 Internal Processes as Markers of Runaway Acceleration Onset

Geodetic observations at Insel (Fig. 4C1) indicate that irreversible acceleration consistent with tertiary creep had already emerged before 2023 (Loew et al., 2025b). The seismically identified transition 37 days before the 15 June collapse therefore does not mark the onset of tertiary creep itself, but rather a transition within the broader tertiary regime from externally modulated deformation to internally sustained acceleration. This suggests that internal feedback mechanisms progressively strengthened over time before evolving into a self-sustaining acceleration phase that became effectively independent of rainfall forcing.

Operational early-warning systems critically depend on distinguishing the onset of sustained tertiary creep from transient accelerations occurring during secondary creep. However, transient accelerations during secondary creep, often driven by external forcings such as rainfall, can be misinterpreted as the onset of tertiary failure in empirical failure-time forecasting models (Fukuzono, 1985b; Voight, 1988b). Such misclassification can bias forecasts, leading to underestimated critical velocity thresholds and premature failure-time predictions that are not sustained once deformation subsequently decelerates or stabilizes (Crosta & Agliardi, 2003b; Leinauer et al., 2023). Recent approaches attempt to identify tertiary acceleration as a statistical anomaly within long-term velocity records of secondary creep (Lei et al., 2023). In practice, however, such extended high-quality datasets are rarely available prior to failure. Moreover, the identification of regime transitions is inherently scale-dependent, as the apparent curvature of displacement and velocity time series varies with the observation window, complicating a robust distinction between secondary and tertiary behaviour. These limitations highlight a fundamental challenge: detecting the onset of internally driven runaway deformation from short, evolving time series without prior knowledge of the system's long-term evolution. In this study, we identify two diagnostic markers of this transition from joint seismic and kinematic observations: (1) a driver–response decoupling, marked by accelerated subsurface seismicity independent of external forcing, indicating the emergence of self-sustained feedbacks; and (2) a relative increase in slip compared to seismicity, reflecting frictional weakening and progressively more efficient sliding. While the broader applicability of these indicators remains to be evaluated across other landslides, the observations presented here provide new insight into how the transition from externally influenced acceleration to internally sustained runaway deformation may be identified, thereby contributing to a key challenge in operational early-warning systems.

6 Conclusions

Slow-moving landslides can transition to catastrophic acceleration with little warning, sometimes even in the absence of obvious external forcing. Distinguishing the onset of internally driven runaway acceleration from reversible, rainfall-induced transient acceleration remains a central challenge for hazard forecasting, particularly because critical processes at depth may not be expressed at the surface. At Brienz/Brinzauls, Using seismic montioring and supverpised machine learning based event picking, we track evolution of subsurface micro-quakes at depth as well as rockfalls emerging from the moving mass. We identify a clear transition from an externally controlled regime, in which rainfall-driven increases in deformation and seismicity decayed once forcing subsided, to an internally driven regime approximately 37 days before collapse. At this transition, subsurface seismicity began accelerating nearly 48 hours before the next rainfall event, and both sliding rates and microseismic activity continued to accelerate under dry conditions. A key characteristic of this phase was increasingly efficient sliding, whereby displacement accumulated faster than seismic cracking, suggesting declining resistance along the failure surface. With a delay of approximately 9 days, the ratio of surface rockfalls to subsurface microseismic events progressively increased, indicating progressive degradation of the mechanical integrity of the moving rock mass. By resolving subsurface deformation processes at high temporal resolution, seismic observations can identify critical transitions within otherwise continuously accelerating instabilities that may not be apparent from surface kinematics alone. Integrated with geodetic measurements, such observations have the potential to improve early-warning systems.

7 Software and Data Availability

The seismic data used in this study are publicly available through GFZ Data Services (DOI: 10.14470/81964787). This study also makes use of the open-access Brienz/Brinzauls Insel Compartment dataset published by ETH Zurich, specifically the terrestrial positioning system (TPS) displacement measurements and local meteorological observations (DOI: 10.3929/ethz-b-000670494). Clustering of repeating seismic events was performed using REDPy (Version 1.1.3; Hotovec-Ellis, 2025; `https://doi.org/10.5066/P13SRZTC`). Data processing and visualization were carried out using Spyder, Jupyter Notebook, and RStudio.

8 Acknowledgments

This project received funding from the European Union's Horizon Europe Marie Skłodowska-Curie Actions Doctoral Network EnvSeis under Grant Agreement No. 101073148. We gratefully acknowledge Gunnar Pruß for field support and the maintenance of the seismic monitoring network. We thank Luc Illien, Simon Loew, Georg Dresen, and Piero Poli for valuable discussions and scientific insights that contributed to this work. Scientific colour maps developed by F. Crameri (Crameri, 2023) were used in this study. The authors used large language model (LLM) tools during manuscript preparation to assist with code optimization and English-language editing. All outputs generated by these tools were critically reviewed, verified, and revised by the authors, who take full responsibility for the content of this publication.

References

Agliardi, F., Scuderi, M. M., Fusi, N., & Collettini, C. (2020a). Slow-to-fast transition of giant creeping rockslides modulated by undrained loading in basal shear zones. *Nature Communications*, *11*, 1352. doi: 10.1038/s41467-020-15093-3

Agliardi, F., Scuderi, M. M., Fusi, N., & Collettini, C. (2020b, March). Slow-to-fast transition of giant creeping rockslides modulated by undrained load-

ing in basal shear zones. *Nature Communications*, *11*(1), 1352. doi: 10.1038/s41467-020-15093-3

Allen, R. V. (1978, October). Automatic earthquake recognition and timing from single traces. *Bulletin of the Seismological Society of America*, *68*(5), 1521–1532. doi: 10.1785/BSSA0680051521

Amitrano, D., & Helmstetter, A. (2006, November). Brittle creep, damage, and time to failure in rocks. *Journal of Geophysical Research: Solid Earth*, *111*(B11), 2005JB004252. doi: 10.1029/2005JB004252

Aspaas, A., Lacroix, P., Sena, C., Kristensen, L., Langet, N., & Renard, F. (2024). Creep Bursts on the Åknes Landslide, Norway: Detection, Characterization and Possible Mechanisms. *Journal of Geophysical Research: Earth Surface*, *129*(12), e2024JF007733. doi: 10.1029/2024JF007733

Bontemps, N., Lacroix, P., Larose, E., Jara, J., & Taipe, E. (2020). Rain and small earthquakes maintain a slow-moving landslide in a persistent critical state. *Nature Communications*, *11*, 780. doi: 10.1038/s41467-020-14445-3

Borgeat, X., Glueer, F., Häusler, M., Hobiger, M., & Fäh, D. (2024, November). On the variability of the site-response parameters of the active rock slope in Brienz/Brinzauls (Switzerland). *Geophysical Journal International*, *240*(1), 779–790. doi: 10.1093/gji/ggae412

Brace, W. F., & Byerlee, J. D. (1966, August). Stick-Slip as a Mechanism for Earthquakes. *Science*, *153*(3739), 990–992. doi: 10.1126/science.153.3739.990

Brantut, N., Heap, M. J., Meredith, P. G., & Baud, P. (2013a). Time-dependent cracking and brittle creep in crustal rocks: A review. *Journal of Structural Geology*, *52*, 17–43. doi: 10.1016/j.jsg.2013.03.007

Brantut, N., Heap, M. J., Meredith, P. G., & Baud, P. (2013b, July). Time-dependent cracking and brittle creep in crustal rocks: A review. *Journal of Structural Geology*, *52*, 17–43. doi: 10.1016/j.jsg.2013.03.007

Burtin, A., Hovius, N., & Turowski, J. M. (2016a, April). Seismic monitoring of torrential and fluvial processes. *Earth Surface Dynamics*, *4*(2), 285–307. doi: 10.5194/esurf-4-285-2016

Burtin, A., Hovius, N., & Turowski, J. M. (2016b, April). Seismic monitoring of torrential and fluvial processes. *Earth Surface Dynamics*, *4*(2), 285–307. doi: 10.5194/esurf-4-285-2016

Carey, J. M., Massey, C. I., Lyndsell, B., & Petley, D. N. (2019, August). Displacement mechanisms of slow-moving landslides in response to changes in porewater pressure and dynamic stress. *Earth Surface Dynamics*, *7*(3), 707–722. doi: 10.5194/esurf-7-707-2019

Chang, C., Noda, H., Xu, Q., Huang, D., & Yamaguchi, T. (2024, December). Slow-to-Fast Transition and Shear Localization in Accelerating Creep of Clayey Soil. *Geophysical Research Letters*, *51*(23), e2024GL111839. doi: 10.1029/2024GL111839

Chen, T., & Guestrin, C. (2016). XGBoost: A scalable tree boosting system. In *Proceedings of the 22nd ACM SIGKDD international conference on knowledge discovery and data mining* (pp. 785–794). doi: 10.1145/2939672.2939785

Cook, K. L., Rekapalli, R., Dietze, M., Pilz, M., Cesca, S., Rao, N. P., ... Hovius, N. (2021, October). Detection and potential early warning of catastrophic flow events with regional seismic networks. *Science*, *374*(6563), 87–92. doi: 10.1126/science.abj1227

Corcoran, J., & Davies, C. (2018, May). Monitoring power-law creep using the Failure Forecast Method. *International Journal of Mechanical Sciences*, *140*, 179–188. doi: 10.1016/j.ijmecsci.2018.02.041

Crameri, F. (2023, October). *Scientific colour maps.* Zenodo. doi: 10.5281/ZENODO.1243862

Crosta, G. B., & Agliardi, F. (2003a, February). Failure forecast for large rock slides

by surface displacement measurements. *Canadian Geotechnical Journal*, *40*(1), 176–191. doi: 10.1139/t02-085

Crosta, G. B., & Agliardi, F. (2003b, February). Failure forecast for large rock slides by surface displacement measurements. *Canadian Geotechnical Journal*, *40*(1), 176–191. doi: 10.1139/t02-085

Dietze, M. (2018, August). The R package "eseis" – a software toolbox for environmental seismology. *Earth Surface Dynamics*, *6*(3), 669–686. doi: 10.5194/esurf-6-669-2018

Dietze, M., Krautblatter, M., Illien, L., & Hovius, N. (2021a, February). Seismic constraints on rock damaging related to a failing mountain peak: The Hochvogel, Allgäu. *Earth Surface Processes and Landforms*, *46*(2), 417–429. doi: 10.1002/esp.5034

Dietze, M., Krautblatter, M., Illien, L., & Hovius, N. (2021b, February). Seismic constraints on rock damaging related to a failing mountain peak: The Hochvogel, Allgäu. *Earth Surface Processes and Landforms*, *46*(2), 417–429. doi: 10.1002/esp.5034

Dietze, M., Mohadjer, S., Turowski, J. M., Ehlers, T. A., & Hovius, N. (2017, October). Seismic monitoring of small alpine rockfalls – validity, precision and limitations. *Earth Surface Dynamics*, *5*(4), 653–668. doi: 10.5194/esurf-5-653-2017

Dilley, M., Chen, R. S., Deichmann, U., Lerner-Lam, A. L., & Arnold, M. (2012). *Natural Disaster Hotspots: A Global Risk Analysis.* Washington, DC: World Bank.

Dutler, N., Valley, B., Gischig, V., Jalali, M., Brixel, B., Krietsch, H., ... Amann, F. (2020, November). Hydromechanical insight of fracture opening and closure during in-situ hydraulic fracturing in crystalline rock. *International Journal of Rock Mechanics and Mining Sciences*, *135*, 104450. doi: 10.1016/j.ijrmms.2020.104450

Ehrlich, D., Melchiorri, M., & Capitani, C. (2021). Population trends and urbanisation in mountain ranges of the world. *Land*, *10*(3), 255. doi: 10.3390/land10030255

Faillettaz, J., Sornette, D., & Funk, M. (2010a). Gravity-driven instabilities: Interplay between state- and velocity-dependent frictional sliding and stress corrosion damage cracking. *Journal of Geophysical Research: Solid Earth*, *115*(B3). doi: 10.1029/2009JB006512

Faillettaz, J., Sornette, D., & Funk, M. (2010b, March). Gravity-driven instabilities: Interplay between state- and velocity-dependent frictional sliding and stress corrosion damage cracking. *Journal of Geophysical Research: Solid Earth*, *115*(B3), 2009JB006512. doi: 10.1029/2009JB006512

Ferri, F., Di Toro, G., Hirose, T., Han, R., Noda, H., Shimamoto, T., ... De Rossi, N. (2011, September). Low- to high-velocity frictional properties of the clay-rich gouges from the slipping zone of the 1963 Vaiont slide, northern Italy. *Journal of Geophysical Research*, *116*(B9), B09208. doi: 10.1029/2011JB008338

Figi, D., Thöny, R., Breitenmoser, T., Brunold, F., & Schwestermann, T. (n.d.). Rutschung Brienz/Brinzauls (GR): Geologisch-kinematisches und hydrogeologisches Modell.

Finnegan, N. J., Brodsky, E. E., Savage, H. M., Nereson, A. L., & Murphy, C. R. (2022). Seasonal Slow Landslide Displacement Is Accommodated by mm-Scale Stick-Slip Events. *Geophysical Research Letters*, *49*(20), e2022GL099548. doi: 10.1029/2022GL099548

Finnegan, N. J., Perkins, J. P., Nereson, A. L., & Handwerger, A. L. (2021, May). Unsaturated Flow Processes and the Onset of Seasonal Deformation in Slow-Moving Landslides. *Journal of Geophysical Research: Earth Surface*, *126*(5), e2020JF005758. doi: 10.1029/2020JF005758

Froude, M. J., & Petley, D. N. (2018, August). Global fatal landslide occurrence from 2004 to 2016. *Natural Hazards and Earth System Sciences*, *18*(8), 2161–2181.

doi: 10.5194/nhess-18-2161-2018

Fukuzono, T. (1985a). A Method to Predict the Time of Slope Failure Caused by Rainfall Using the Inverse Number of Velocity of Surface Displacement. *Landslides*, *22*(2), 8-13_1. doi: 10.3313/jls1964.22.2_8

Fukuzono, T. (1985b). A Method to Predict the Time of Slope Failure Caused by Rainfall Using the Inverse Number of Velocity of Surface Displacement. *Landslides*, *22*(2), 8-13_1. doi: 10.3313/jls1964.22.2_8

Geopraevent. (2022). *Monitoring systems for gravitative natural hazards* (Tech. Rep.). Geopraevent.

Gischig, V. S., Moore, J. R., Evans, K. F., Amann, F., & Loew, S. (2011, October). Thermomechanical forcing of deep rock slope deformation: 1. Conceptual study of a simplified slope. *Journal of Geophysical Research*, *116*(F4), F04010. doi: 10.1029/2011JF002006

Goebel, T. H. W., Schuster, V., Kwiatek, G., Pandey, K., & Dresen, G. (2024, July). A laboratory perspective on accelerating preparatory processes before earthquakes and implications for foreshock detectability. *Nature Communications*, *15*(1), 5588. doi: 10.1038/s41467-024-49959-7

Guérin-Marthe, S., Kwiatek, G., Wang, L., Bonnelye, A., Martínez-Garzón, P., & Dresen, G. (2023, April). Preparatory Slip in Laboratory Faults: Effects of Roughness and Load Point Velocity. *Journal of Geophysical Research: Solid Earth*, *128*(4), e2022JB025511. doi: 10.1029/2022JB025511

Guglielmi, Y., Cook, P., Soom, F., Schoenball, M., Dobson, P., & Kneafsey, T. (2021). In Situ Continuous Monitoring of Borehole Displacements Induced by Stimulated Hydrofracture Growth. *Geophysical Research Letters*, *48*(4), e2020GL090782. doi: 10.1029/2020GL090782

Handwerger, A. L., Huang, M.-H., Fielding, E. J., Booth, A. M., & Bürgmann, R. (2019, February). A shift from drought to extreme rainfall drives a stable landslide to catastrophic failure. *Scientific Reports*, *9*(1), 1569. doi: 10.1038/s41598-018-38300-0

Handwerger, A. L., Rempel, A. W., Skarbek, R. M., Roering, J. J., & Hilley, G. E. (2016a, September). Rate-weakening friction characterizes both slow sliding and catastrophic failure of landslides. *Proceedings of the National Academy of Sciences*, *113*(37), 10281–10286. doi: 10.1073/pnas.1607009113

Handwerger, A. L., Rempel, A. W., Skarbek, R. M., Roering, J. J., & Hilley, G. E. (2016b, September). Rate-weakening friction characterizes both slow sliding and catastrophic failure of landslides. *Proceedings of the National Academy of Sciences*, *113*(37), 10281–10286. doi: 10.1073/pnas.1607009113

Handwerger, A. L., Roering, J. J., & Schmidt, D. A. (2013, September). Controls on the seasonal deformation of slow-moving landslides. *Earth and Planetary Science Letters*, *377–378*, 239–247. doi: 10.1016/j.epsl.2013.06.047

Helmstetter, A., & Garambois, S. (2010). Seismic monitoring of Séchilienne rockslide (French Alps): Analysis of seismic signals and their correlation with rainfalls. *Journal of Geophysical Research: Earth Surface*, *115*(F3). doi: 10.1029/2009JF001532

Helmstetter, A., Sornette, D., Grasso, J.-R., Andersen, J. V., Gluzman, S., & Pisarenko, V. (2004, February). Slider block friction model for landslides: Application to Vaiont and La Clapière landslides. *Journal of Geophysical Research: Solid Earth*, *109*(B2), 2002JB002160. doi: 10.1029/2002JB002160

Hibert, C., Mangeney, A., Grandjean, G., Baillard, C., Rivet, D., Shapiro, N. M., ... Crawford, W. (2014). Automated identification, location, and volume estimation of rockfalls at Piton de la Fournaise volcano. *Journal of Geophysical Research: Earth Surface*, *119*(5), 1082–1105. doi: 10.1002/2013JF002970

Hotovec-Ellis, A. J. (2025, November). REDPy: A Python Tool for Automated Repeating Earthquake Detection and Visualization. *Seismological Research Letters*,

96(6), 3849–3865. doi: 10.1785/0220240373

Hotovec-Ellis, A. J. (2025, June). REDPy: A Python Tool for Automated Repeating Earthquake Detection and Visualization. *Seismological Research Letters*, *96*(6), 3849–3865. doi: 10.1785/0220240373

Hungr, O., Leroueil, S., & Picarelli, L. (2014). The Varnes classification of landslide types, an update. *Landslides*, *11*(2), 167–194. doi: 10.1007/s10346-013-0436-y

Incorporated Research Institutions for Seismology (IRIS). (2023). *IRIS federation of digital seismograph networks (FDSN) web service.* IRIS Data Services.

Intrieri, E., Carlà, T., & Gigli, G. (2019, June). Forecasting the time of failure of landslides at slope-scale: A literature review. *Earth-Science Reviews*, *193*, 333–349. doi: 10.1016/j.earscirev.2019.03.019

Jaffar, Q., Zhou, Q., & Tang, H. (2024, April). Detecting Mass Movements using Fractal-based algorithm. In *European Geosciences Union General Assembly 2024 (EGU24)* (p. 12171). doi: 10.5194/egusphere-egu24-12171

Kang, J., Walter, F., Paitz, P., Aichele, J., Edme, P., Meier, L., & Fichtner, A. (2024a). Automatic Monitoring of Rock-Slope Failures Using Distributed Acoustic Sensing and Semi-Supervised Learning. *Geophysical Research Letters*, *51*(19), e2024GL110672. doi: 10.1029/2024GL110672

Kang, J., Walter, F., Paitz, P., Aichele, J., Edme, P., Meier, L., & Fichtner, A. (2024b, October). Automatic Monitoring of Rock-Slope Failures Using Distributed Acoustic Sensing and Semi-Supervised Learning. *Geophysical Research Letters*, *51*(19), e2024GL110672. doi: 10.1029/2024GL110672

Kemeny, J. (2003, January). The Time-Dependent Reduction of Sliding Cohesion due to Rock Bridges Along Discontinuities: A Fracture Mechanics Approach. *Rock Mechanics and Rock Engineering*, *36*(1), 27–38. doi: 10.1007/s00603-002-0032-2

Kenner, R., Schwestermann, T., Thöny, R., Figi, D., Stoffel, A., Bühler, Y., ... Manconi, A. (2025, October). Formation phases and structural failure of a landslide compartment at Brienz/Brinzauls, Switzerland. *Engineering Geology*, *357*, 108343. doi: 10.1016/j.enggeo.2025.108343

Kilburn, C. R., & Petley, D. N. (2003, August). Forecasting giant, catastrophic slope collapse: Lessons from Vajont, Northern Italy. *Geomorphology*, *54*(1-2), 21–32. doi: 10.1016/S0169-555X(03)00052-7

Kilburn, C. R. J., & Petley, D. N. (2003, August). Forecasting giant, catastrophic slope collapse: Lessons from Vajont, Northern Italy. *Geomorphology*, *54*(1), 21–32. doi: 10.1016/S0169-555X(03)00052-7

Kirschbaum, D., Kapnick, S. B., Stanley, T., & Pascale, S. (2020, February). Changes in Extreme Precipitation and Landslides Over High Mountain Asia. *Geophysical Research Letters*, *47*(4), e2019GL085347. doi: 10.1029/2019GL085347

Kjekstad, O., & Highland, L. (2009). Economic and Social Impacts of Landslides. In K. Sassa & P. Canuti (Eds.), *Landslides – Disaster Risk Reduction* (pp. 573–587). Berlin, Heidelberg: Springer Berlin Heidelberg. doi: 10.1007/978-3-540-69970-5_30

Krähenbühl, R., & Nänni, C. (2017). Ist das Dorf Brienz-Brinzauls Bergsturz gefährdet?
doi: 10.5169/SEALS-738126

Lacroix, P., & Helmstetter, A. (2011, February). Location of Seismic Signals Associated with Microearthquakes and Rockfalls on the Séchilienne Landslide, French Alps. *Bulletin of the Seismological Society of America*, *101*(1), 341–353. doi: 10.1785/0120100110

Lagarde, S., Dietze, M., Hammer, C., Zeckra, M., Voigtländer, A., Illien, L., ... Turowski, J. M. (2023, June). Rock slope failure preparation paced by total crack boundary length. *Communications Earth & Environment*, *4*(1), 201. doi: 10.1038/s43247-023-00851-0

Lei, Q., Sornette, D., Yang, H., & Loew, S. (2023, March). Real-Time Forecast of Catastrophic Landslides via Dragon-King Detection. *Geophysical Research Letters*, *50*(6), e2022GL100832. doi: 10.1029/2022GL100832

Leinauer, J., Weber, S., Cicoira, A., Beutel, J., & Krautblatter, M. (2023, July). An approach for prospective forecasting of rock slope failure time. *Communications Earth & Environment*, *4*(1), 253. doi: 10.1038/s43247-023-00909-z

Loche, M., Scaringi, G., Yunus, A. P., Catani, F., Tanyaş, H., Frodella, W., ... Lombardo, L. (2022, January). Surface temperature controls the pattern of post-earthquake landslide activity. *Scientific Reports*, *12*(1), 988. doi: 10.1038/s41598-022-04992-8

Loew, S. (2024, April). *Monitoring Data from the Insel Compartment at Brienz/Brinzauls Switzerland: Basic Data Set related the Summary Article of Loew et al. 2024.* ETH Zurich. doi: 10.3929/ETHZ-B-000670494

Loew, S., Schneider, S., Josuran, M., Figi, D., Thoeny, R., Huwiler, A., ... Naenni, C. (2025a, February). Early warning and dynamics of compound rockslides: Lessons learnt from the Brienz/Brinzauls 2023 rockslope failure. *Landslides*, *22*(2), 283–298. doi: 10.1007/s10346-024-02380-z

Loew, S., Schneider, S., Josuran, M., Figi, D., Thoeny, R., Huwiler, A., ... Naenni, C. (2025b, February). Early warning and dynamics of compound rockslides: Lessons learnt from the Brienz/Brinzauls 2023 rockslope failure. *Landslides*, *22*(2), 283–298. doi: 10.1007/s10346-024-02380-z

Loew, S., Schneider, S., Josuran, M., Figi, D., Thoeny, R., Huwiler, A., ... Naenni, C. (2025c, February). Early warning and dynamics of compound rockslides: Lessons learnt from the Brienz/Brinzauls 2023 rockslope failure. *Landslides*, *22*(2), 283–298. doi: 10.1007/s10346-024-02380-z

Lombardo, L., Bakka, H., Tanyas, H., Van Westen, C., Mai, P. M., & Huser, R. (2019, July). Geostatistical Modeling to Capture Seismic-Shaking Patterns From Earthquake-Induced Landslides. *Journal of Geophysical Research: Earth Surface*, *124*(7), 1958–1980. doi: 10.1029/2019JF005056

Main, I. G. (2000, July). A damage mechanics model for power-law creep and earthquake aftershock and foreshock sequences. *Geophysical Journal International*, *142*(1), 151–161. doi: 10.1046/j.1365-246x.2000.00136.x

Manconi, A. (2021, June). How phase aliasing limits systematic space-borne DInSAR monitoring and failure forecast of alpine landslides. *Engineering Geology*, *287*, 106094. doi: 10.1016/j.enggeo.2021.106094

Manconi, A., Jones, N., Loew, S., Strozzi, T., Caduff, R., & Wegmueller, U. (2024, October). Monitoring surface deformation with spaceborne radar interferometry in landslide complexes: Insights from the Brienz/Brinzauls slope instability, Swiss Alps. *Landslides*, *21*(10), 2519–2533. doi: 10.1007/s10346-024-02291-z

Markatou, M., Tian, H., Biswas, S., & Hripcsak, G. (n.d.). Analysis of Variance of Cross-Validation Estimators of the Generalization Error.

Meng, F., Wang, F., Wong, L. N. Y., Song, J., Li, M., Zhang, C., & Zhang, L. (2024, April). Shear behavior and off-fault damage of saw-cut smooth and tension-induced rough joints in granite. *Journal of Rock Mechanics and Geotechnical Engineering*, *16*(4), 1216–1230. doi: 10.1016/j.jrmge.2023.07.008

Moretto, S., Bozzano, F., & Mazzanti, P. (2021, September). The Role of Satellite InSAR for Landslide Forecasting: Limitations and Openings. *Remote Sensing*, *13*(18), 3735. doi: 10.3390/rs13183735

Nadeau, R. M., & McEvilly, T. V. (1999, July). Fault Slip Rates at Depth from Recurrence Intervals of Repeating Microearthquakes. *Science*, *285*(5428), 718–721. doi: 10.1126/science.285.5428.718

Noël, C., Giorgetti, C., Scuderi, M. M., Collettini, C., & Marone, C. (2023a). The Effect of Shear Displacement and Wear on Fault Stability: Laboratory Constraints. *Journal of Geophysical Research: Solid Earth*, *128*(4), e2022JB026191.

doi: 10.1029/2022JB026191

Noël, C., Giorgetti, C., Scuderi, M. M., Collettini, C., & Marone, C. (2023b, April). The Effect of Shear Displacement and Wear on Fault Stability: Laboratory Constraints. *Journal of Geophysical Research: Solid Earth*, *128*(4), e2022JB026191. doi: 10.1029/2022JB026191

Patton, A. I., Rathburn, S. L., & Capps, D. M. (2019). Landslide response to climate change in permafrost regions. *Geomorphology*, *340*. doi: 10.1016/j.geomorph .2019.04.029

Paul, K., Bhattacharya, P., & Misra, S. (2024a). Frictional Control on Accelerating Creep During the Slow-To-Fast Transition of Rainfall-Induced Catastrophic Landslides. *Journal of Geophysical Research: Earth Surface*, *129*(1), e2023JF007213. doi: 10.1029/2023JF007213

Paul, K., Bhattacharya, P., & Misra, S. (2024b, January). Frictional Control on Accelerating Creep During the Slow-To-Fast Transition of Rainfall-Induced Catastrophic Landslides. *Journal of Geophysical Research: Earth Surface*, *129*(1), e2023JF007213. doi: 10.1029/2023JF007213

Petley, D. (2012). Global patterns of loss of life from landslides. *Geology*, *40*. doi: 10.1130/G33217.1

Poli, P. (2017a). Creep and slip: Seismic precursors to the Nuugaatsiaq landslide (Greenland). *Geophysical Research Letters*, *44*(17), 8832–8836. doi: 10.1002/ 2017GL075039

Poli, P. (2017b, September). Creep and slip: Seismic precursors to the Nuugaatsiaq landslide (Greenland). *Geophysical Research Letters*, *44*(17), 8832–8836. doi: 10 .1002/2017GL075039

Provost, F., Hibert, C., & Malet, J.-P. (2017a). Automatic classification of endogenous landslide seismicity using the Random Forest supervised classifier. *Geophysical Research Letters*, *44*(1), 113–120. doi: 10.1002/2016GL070709

Provost, F., Hibert, C., & Malet, J.-P. (2017b, January). Automatic classification of endogenous landslide seismicity using the Random Forest supervised classifier. *Geophysical Research Letters*, *44*(1), 113–120. doi: 10.1002/2016GL070709

Provost, F., Malet, J.-P., Hibert, C., Helmstetter, A., Radiguet, M., Amitrano, D., ... Vial, B. (2018, November). Towards a standard typology of endogenous landslide seismic sources. *Earth Surface Dynamics*, *6*(4), 1059–1088. doi: 10.5194/esurf-6-1059-2018

Renard, F., McBeck, J., & Cordonnier, B. (2020, May). Competition between slow slip and damage on and off faults revealed in 4D synchrotron imaging experiments. *Tectonophysics*, *782–783*, 228437. doi: 10.1016/j.tecto.2020.228437

Sattar, A., Cook, K. L., Rai, S. K., Berthier, E., Allen, S., Rinzin, S., ... Bhat, S. Y. (2025, March). The Sikkim flood of October 2023: Drivers, causes, and impacts of a multihazard cascade. *Science*, *387*(6740), eads2659. doi: 10.1126/science.ads2659

Schneider, M., Oestreicher, N., Ehrat, T., & Loew, S. (2023a, November). Rockfall monitoring with a Doppler radar on an active rockslide complex in Brienz/Brinzauls (Switzerland). *Natural Hazards and Earth System Sciences*, *23*(11), 3337–3354. doi: 10.5194/nhess-23-3337-2023

Schneider, M., Oestreicher, N., Ehrat, T., & Loew, S. (2023b, November). Rockfall monitoring with a Doppler radar on an active rockslide complex in Brienz/Brinzauls (Switzerland). *Natural Hazards and Earth System Sciences*, *23*(11), 3337–3354. doi: 10.5194/nhess-23-3337-2023

Schöpa, A., Chao, W.-A., Lipovsky, B. P., Hovius, N., White, R. S., Green, R. G., & Turowski, J. M. (2018a, June). Dynamics of the Askja caldera July 2014 landslide, Iceland, from seismic signal analysis: Precursor, motion and aftermath. *Earth Surface Dynamics*, *6*(2), 467–485. doi: 10.5194/esurf-6-467-2018

Schöpa, A., Chao, W.-A., Lipovsky, B. P., Hovius, N., White, R. S., Green, R. G., & Turowski, J. M. (2018b, June). Dynamics of the Askja caldera July 2014 landslide, Iceland, from seismic signal analysis: Precursor, motion and aftermath. *Earth Surface Dynamics*, *6*(2), 467–485. doi: 10.5194/esurf-6-467-2018

Seydoux, L., Balestriero, R., Poli, P., Hoop, M. D., Campillo, M., & Baraniuk, R. (2020, August). Clustering earthquake signals and background noises in continuous seismic data with unsupervised deep learning. *Nature Communications*, *11*(1), 3972. doi: 10.1038/s41467-020-17841-x

Siblini, W., Fréry, J., He-Guelton, L., Oblé, F., & Wang, Y.-Q. (2020). Master Your Metrics with Calibration. In M. R. Berthold, A. Feelders, & G. Krempl (Eds.), *Advances in Intelligent Data Analysis XVIII* (pp. 457–469). Cham: Springer International Publishing. doi: 10.1007/978-3-030-44584-3_36

Sornette, D., Helmstetter, A., Andersen, J., Gluzman, S., Grasso, J.-R., & Pisarenko, V. (2004, July). Towards landslide predictions: Two case studies. *Physica A: Statistical Mechanics and its Applications*, *338*(3-4), 605–632. doi: 10.1016/j.physa.2004.02.065

Tiwari, A., Sain, K., Kumar, A., Tiwari, J., Paul, A., Kumar, N., ... Pandey, C. P. (2022, March). Potential seismic precursors and surficial dynamics of a deadly Himalayan disaster: An early warning approach. *Scientific Reports*, *12*(1), 3733. doi: 10.1038/s41598-022-07491-y

Voight, B. (1988a, March). A method for prediction of volcanic eruptions. *Nature*, *332*(6160), 125–130. doi: 10.1038/332125a0

Voight, B. (1988b, March). A method for prediction of volcanic eruptions. *Nature*, *332*(6160), 125–130. doi: 10.1038/332125a0

Voigtländer, A., Leith, K., & Krautblatter, M. (2018, May). Subcritical Crack Growth and Progressive Failure in Carrara Marble Under Wet and Dry Conditions. *Journal of Geophysical Research: Solid Earth*, *123*(5), 3780–3798. doi: 10.1029/2017JB014956

Wang, H. F., Bonner, B. P., Carlson, S. R., Kowallis, B. J., & Heard, H. C. (1989, February). Thermal stress cracking in granite. *Journal of Geophysical Research: Solid Earth*, *94*(B2), 1745–1758. doi: 10.1029/JB094iB02p01745

Wang, T., Bian, Y., Zhang, Y., & Hou, X. (2023, January). Classification of earthquakes, explosions and mining-induced earthquakes based on XGBoost algorithm. *Computers & Geosciences*, *170*, 105242. doi: 10.1016/j.cageo.2022.105242

Weber, S., Faillettaz, J., Meyer, M., Beutel, J., & Vieli, A. (2018). Acoustic and microseismic characterization in steep bedrock permafrost on Matterhorn (CH). *J. Geophys. Res.*, *123*. doi: 10.1029/2018JF004615

Yamada, M., Mori, J., & Matsushi, Y. (2016a). Possible stick-slip behavior before the Rausu landslide inferred from repeating seismic events. *Geophysical Research Letters*, *43*(17), 9038–9044. doi: 10.1002/2016GL069288

Yamada, M., Mori, J., & Matsushi, Y. (2016b, September). Possible stick-slip behavior before the Rausu landslide inferred from repeating seismic events. *Geophysical Research Letters*, *43*(17), 9038–9044. doi: 10.1002/2016GL069288

Zhang, T., Ji, J., Liao, W., Cui, H., & Zhang, W. (2024, January). Seismically progressive motion mechanism of earth slopes considering shear band porewater pressure feedback under earthquake excitations. *Computers and Geotechnics*, *165*, 105909. doi: 10.1016/j.compgeo.2023.105909

Zhou, Q., Tang, H., Hibert, C., Chmiel, M., Walter, F., Dietze, M., & Turowski, J. M. (2025, April). Enhancing Debris Flow Warning via Machine Learning Feature Reduction and Model Selection. *Journal of Geophysical Research: Earth Surface*, *130*(4), e2024JF008094. doi: 10.1029/2024JF008094

Table 1: Mean reflector acceleration for different time windows.

Time Window	**V715** (mm/d^2)	**V719** (mm/d^2)	**V725** (mm/d^2)	**Overall Mean** (mm/d^2)
21–23 April	1.3980	1.7121	1.5979	1.5693
26–30 April	1.5854	2.0372	1.7526	1.7917
3–7 May	1.1846	0.2018	1.5095	0.9653
14–18 May	5.2649	9.0543	7.3691	7.2294
18–24 May	6.7993	10.4663	9.1013	8.7890
26–28 May	14.0596	24.2296	19.8230	19.3707

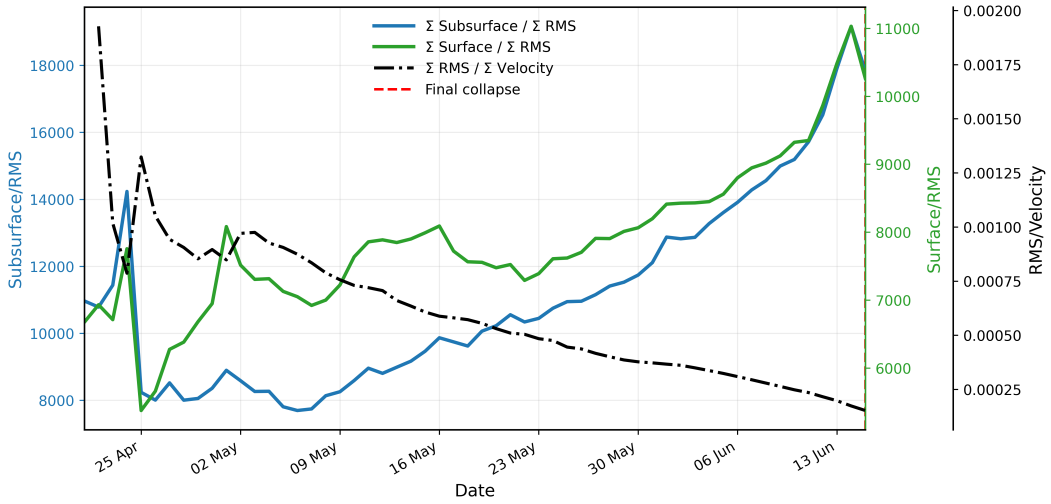

Figure A1: Temporal evolution of cumulative precursor ratios during the 21 April–15 June 2023 acceleration phase preceding the Brienz/Brinzauls collapse. Shown are the ratios between cumulative subsurface seismicity and cumulative seismic RMS amplitude (Σ Subsurface / Σ RMS), cumulative surface seismicity and cumulative RMS (Σ Surface / Σ RMS), and cumulative RMS amplitude and cumulative surface velocity (Σ RMS / Σ Velocity). The dashed red line marks the timing of the final collapse on 15 June 2023.

Appendix A Supplementary precursor ratio analysis

The empirical distribution exhibits a strong excess of short waiting times and a heavy-tailed survival probability extending to several hours, whereas the Poisson expectation decays rapidly by orders of magnitude. This behavior indicates that rockfall occurrence was temporally clustered rather than random, reflecting correlated deformation processes and episodic stress release within the unstable mass.

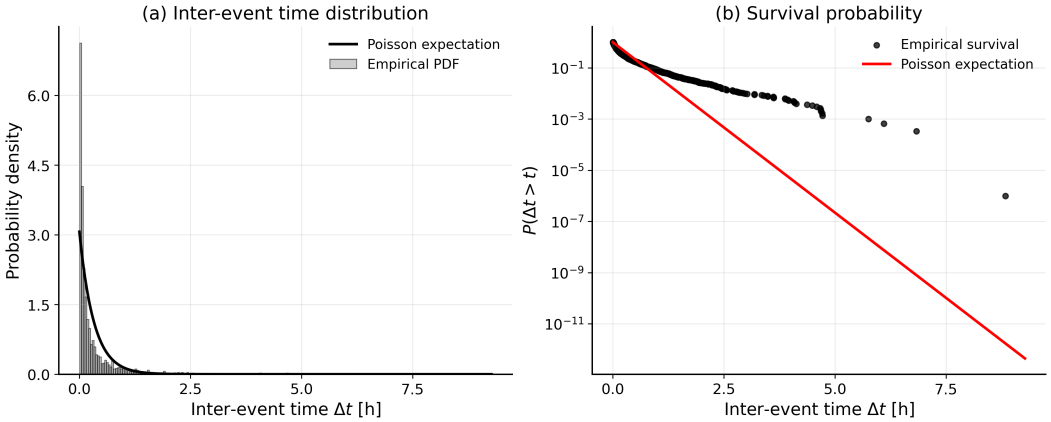

Figure A2: Inter-event time statistics of surface seismicity during the 6 May–15 June 2023 acceleration phase. (a) Empirical inter-event time probability density function compared with the exponential distribution expected for a stationary Poisson process. (b) Empirical survival probability $P(\Delta t > t)$ compared with the corresponding Poisson expectation. Strong deviations from the Poisson model, particularly the heavy-tailed survival behaviour, indicate temporal clustering and non-stationary event occurrence during the acceleration toward collapse.

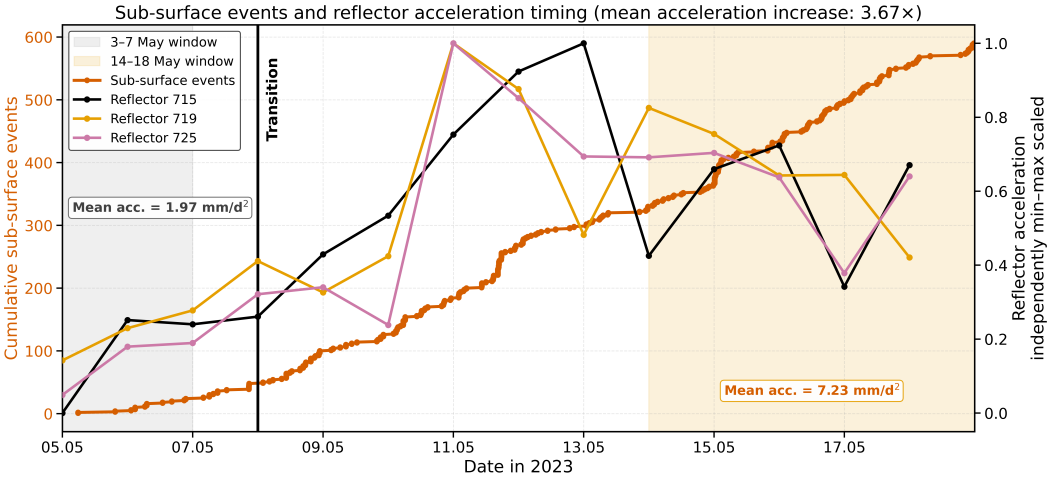

Figure A3: Temporal evolution of cumulative sub-surface seismicity and independently min–max scaled reflector acceleration during the tertiary creep phase. The P4 transition marks the onset of a pronounced acceleration phase, characterized by a ∼4-fold increase in reflector acceleration rate and the initiation of sustained sub-surface seismic acceleration under persistently dry conditions. Shaded intervals denote the pre- and post-P4 acceleration windows, with annotated mean reflector accelerations calculated from Appendix Table 1.

Supplementary Information

This Supplementary Information provides additional methods, robustness analyses, supporting figures, and supplementary tables accompanying the main manuscript.

S1 Methods

S1.1 Preliminary Event Picking and Waveform clustering

We apply a classical Short-Term Average to Long-Term Average (STA–LTA) detector (Allen, 1978) to the continuous seismic record at station BRZ02—the sensor closest to the active deformation zone—to construct an initial pool of potential slope-related and other transient events. At this exploratory stage, completeness is not a priority; the aim is to capture a broad diversity of signal types for subsequent analysis. Prior to detection, we remove the instrument response, de-trend the signal, and apply a 5–15 Hz band-pass filter to the vertical component to suppress background and anthropogenic noise while preserving the frequency range most sensitive to slope seismicity (typically 1–45 Hz; (Provost et al., 2018)). Each waveform reflects both the source mechanism and the effects of wave propagation, so STA–LTA detections are grouped by waveform similarity using REDPy (Repeating Earthquake Detector in Python; (Hotovec-Ellis, 2025), Version 1.1.3). REDPy extracts representative templates from the triggered detections and clusters similar signals into families of repeating sources based on waveform cross-correlation. We process all nine channels from BRZ02, BRZ03, and BRZ04 using identical STA–LTA settings in REDPy. The trigger window is designed to capture short, impulsive sources: a 0.5 s STA, a 180 s LTA, and a trigger ratio of 5 with a de-trigger ratio of 2. Based on our observations that crack events typically last 2–5 s, we use a 256-sample waveform window and apply a 1–10 Hz band-pass filter to suppress rapidly attenuating high-frequency noise that might reduce waveform similarity. We retain detections that trigger on at least five of the nine channels. For event association into repeating families, we require a minimum inter-event correlation of 0.8 on at least four channels. Given the short source–receiver distances (500–800 m), these conservative criteria minimize the risk of grouping distinct sources together. We then focus exclusively on repeating families that (i) have their final occurrence before 16 May and (ii) contain at least five members, eliminating small or late-initiating clusters that are not relevant to the acceleration phase of the Insel.

S1.11 Source Location

Event locations were estimated using a signal-migration approach originally developed for the localization of seismic signals generated by geomorphic processes (Burtin et al., 2016b) and is implemented in the R package `eseis` (Dietze, 2018). The approach relies on aligning waveform envelopes across the sensor network and is particularly effective for locating emergent sources. For each station pair, empirical envelope time delays were obtained via cross-correlation. To account for geometric spreading and topography, we generated distance maps on a regular grid surrounding the network using a 30 m resolution DEM, and converted these distance fields into theoretical travel-time grids assuming an apparent seismic velocity. The observed inter-station time delays were then compared with the synthetic time delays predicted at every grid node. This yields a spatial probability distribution of source locations, ranging from 0 to 1, where high values indicate a stronger match between empirical and modeled travel times. Apart from the minimum three stations required for triangulation (BRZ02–BRZ04), we also use BRZ01 to provide additional spatial constraints, but exclude the more distant BRZ12 (1 km

south) because it rarely records the small-amplitude signals originating within the *Insel*.

To assess how the assumed apparent seismic velocity affects source localization, we perform a sensitivity analysis on a well-documented failure at 15:37 local time on 15 June, when a substantial portion of the Insel toe collapses. We manually pick the event onset from spectrograms and define an area of interest (AOI) around the lower Insel. We then repeat the signal-migration procedure for apparent velocities between 100 and 1000 m s^1 in 50 m s^1 increments, allowing us to evaluate how the choice of velocity influences the estimated source position. The corresponding source coordinates were compared to the predefined AOI to determine whether the estimated location fell inside or outside the collapse zone. The distance between the maximum-energy point and the AOI center was then computed for each velocity, producing a velocity–distance relationship.

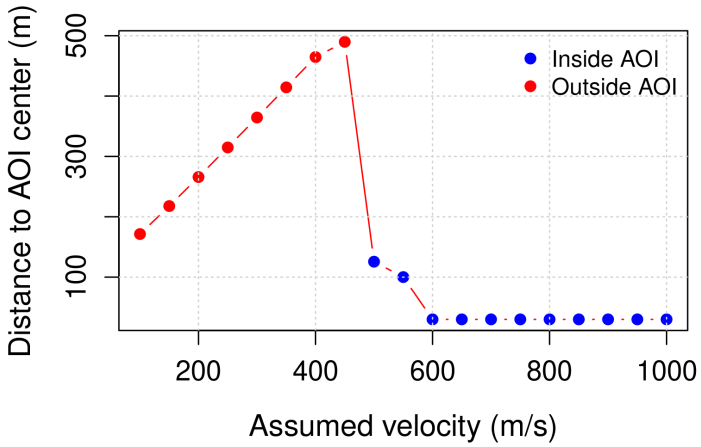

Figure S1: Sensitivity of the migration-derived source position to the assumed seismic wave velocity. Each point represents the distance between the maximum migration energy and the center of the area of interest (AOI) for a given trial velocity. Blue symbols indicate that the maximum-energy location lies within the AOI, while red symbols denote locations outside it. The distance decreases sharply above ∼500 m s^{-1}, beyond which all solutions remain spatially stable within the AOI. This relationship provides a quantitative constraint on the effective propagation velocity that best focuses the migration energy in the observed collapse region.

A total of eight rockfall events were selected from the Doppler-derived rockfall catalog and independently migrated over a range of assumed propagation velocities. To ensure a consistent comparison between events and to focus on the initial high-energy phase of the rockfall signal, only the first 15 s of each event were used for migration, irrespective of the total catalog duration. To evaluate the most plausible migration velocity, we quantified how consistently the independently migrated rockfalls collapsed onto the expected source corridor. Because rockfalls are expected to follow the steepest topographic gradient, the recovered source locations should exhibit minimal lateral (cross-slope) scatter. Assuming that the X-coordinate approximately represents the cross-slope direction, we computed the absolute deviation from the Insel centerline and the inter-event spread of migrated X coordinates for each tested velocity. For each velocity, we calculated the mean, median, maximum, and standard deviation of the X-coordinate deviations from

the Insel center. In addition, we computed robust measures of inter-event scatter including the median absolute deviation (MAD) and interquartile range (IQR). A physically plausible migration velocity should minimize these quantities, indicating that independently located rockfalls converge onto a common source corridor rather than being dispersed laterally across the slope. The results show a pronounced minimum in X-direction scatter at velocities of approximately 400–500 m,s^{-1}. The smallest mean deviation from the Insel center was obtained at 500 m,s^{-1} (124.5 m), closely followed by 400 m,s^{-1} (131.2 m). Likewise, the inter-event standard deviation of migrated X positions reached its minimum at 500 m,s^{-1} (155.6 m), compared with 338.0 m at 200 m,s^{-1} and 472.6 m at 700 m,s^{-1}. Relative to 200 m,s^{-1}, the velocity of 500 m,s^{-1} reduced inter-event X scatter by approximately 54%, while relative to 700 m,s^{-1} the reduction was approximately 67%. These substantial reductions indicate that migration velocities near 500 m,s^{-1} produce markedly more coherent source locations. The convergence of multiple independent rockfalls toward a common cross-slope position strongly suggests that the apparent propagation velocity is best represented by a value in the range of 400–500 m,s^{-1}. Furthermore, because the Insel source area is elongated approximately parallel to the slope direction, the perpendicular distance from migrated locations to the Insel centerline should also be minimized at the correct migration velocity. The observed minimum in X-direction deviation therefore provides an independent geometrical constraint supporting the same preferred velocity range. Overall, both the reduction in inter-event lateral scatter and the minimization of distance from the Insel source corridor consistently indicate an optimal migration velocity of approximately 500 m,s^{-1}.

S1.2 Supervised Classifier Training and Deployment on continuous time series

Model Station	Noise	Surface	Earthquake	Sub-surface
Training Counts (70%)				
BRZ02	46317	21869	6699	1982
BRZ03	36909	21869	926	1982
BRZ04	36909	21868	926	448
Testing Counts (30%)				
BRZ02	19851	9372	2871	850
BRZ03	15818	9372	397	850
BRZ04	15818	9373	397	192

Table S1: Training and testing sample counts (70%-30% split) for the BRZ02, BRZ03, and BRZ04 datasets.

Training Features

#	Feature Name	Definition
Time-Related Features		
1	t_duration	Duration of the signal.
2	t_rise	Signal rise time: time from start to maximum amplitude.
3	t_fall	Signal fall time: time from maximum amplitude to end.
4	t_risefall	Ratio of rise to fall time (t_rise/t_fall).

Continued on next page...

#	Feature Name	Definition
Amplitude and Raw-Signal Statistics		
5	a_skewness	Skewness of the signal amplitude distribution.
6	a_kurtosis	Kurtosis of the signal amplitude distribution.
7	raw_skewness	Skewness of the raw (unprocessed) signal.
8	raw_kurtosis	Kurtosis of the raw (unprocessed) signal.
9	a1_kurtosis	Kurtosis of band-limited amplitude in 0.1–1 Hz.
10	a2_kurtosis	Kurtosis of band-limited amplitude in 1–3 Hz.
11	a3_kurtosis	Kurtosis of band-limited amplitude in 3–10 Hz.
12	a4_kurtosis	Kurtosis of band-limited amplitude in 10–20 Hz.
13	a5_kurtosis	Kurtosis of band-limited amplitude in 20–50 Hz.
Envelope Statistics		
14	e_maxmean	Ratio of maximum to mean envelope value.
15	e_maxmedian	Ratio of maximum to median envelope value.
16	e_skewness	Skewness of the signal envelope distribution.
17	e_kurtosis	Kurtosis of the signal envelope distribution.
18	e1_logsum	log of the summed envelope in 0.1–1 Hz band.
19	e2_logsum	log of the summed envelope in 1–3 Hz band.
20	e3_logsum	log of the summed envelope in 3–10 Hz band.
21	e4_logsum	log of the summed envelope in 10–20 Hz band.
22	e5_logsum	log of the summed envelope in 20–50 Hz band.
23	e_rmsdecphaseline	RMS of envelope residuals from a linear decrease model (departure from linear decay).
24	e_devlinearfall	Deviation of the envelope fall from an ideal linear decrease (envelope fall-shape irregularity).
Cross-Correlation Function Features		
25	c_peaks	Number of peaks in the signal cross-correlation function (excursions above 75% of the maximum).
26	c_energy1	Sum of the first third of the cross-correlation function.
27	c_energy2	Sum of the last two thirds of the cross-correlation function.
28	c_energy3	Ratio $c\_energy1/c\_energy2$.
Spectral Power Statistics		
29	s_peaks	Number of peaks in spectral power (excursions above 75% of the maximum).
30	s_peakpower	Mean power of spectral peaks.
31	s_mean	Mean spectral power.
32	s_median	Median spectral power.
33	s_max	Maximum spectral power.
34	s_var	Variance of the spectral power.
35	s_flatness	Spectral flatness.
36	s_entropy	Spectral entropy.
37	s_precision	Spectral precision (as defined by the spectral-property routine).
38	s_sd	Standard deviation of spectral power.
39	s_sem	Standard error of the mean of spectral power.

Continued on next page...

#	Feature Name	Definition
Band-Limited Spectral Energy		
40	s1_energy	Spectral energy in 0.1–1 Hz band.
41	s2_energy	Spectral energy in 1–3 Hz band.
42	s3_energy	Spectral energy in 3–10 Hz band.
43	s4_energy	Spectral energy in 10–20 Hz band.
44	s5_energy	Spectral energy in 20–30 Hz band.
45	s_gamma1	Gamma 1: spectral centroid.
46	s_gamma2	Gamma 2: spectral gyration radius.
47	s_gamma3	Gamma 3: spectral centroid width.
Frequency-Domain Descriptors		
48	f_modal	Modal frequency.
49	f_mean	Mean (central) frequency.
50	f_median	Median frequency.
51	f_q05	0.05 quantile of the spectrum.
52	f_q25	0.25 quantile of the spectrum.
53	f_q75	0.75 quantile of the spectrum.
54	f_q95	0.95 quantile of the spectrum.
55	f_iqr	Interquartile range of the spectrum.
56	f_centroid	Spectral centroid.
Time-Frequency Peak-Shape Features		
57	p_kurtosismax	Kurtosis of the maximum spectral power over time.
58	p_kurtosismedian	Kurtosis of the median spectral power over time.
59	p_maxmean	Mean over time of the ratio (max / mean) spectral power.
60	p_maxmedian	Mean over time of the ratio (max / median) spectral power.
61	p_peaksmean	Number of peaks in normalised mean spectral power over time.
62	p_peaksmedian	Number of peaks in normalised median spectral power over time.
63	p_peaksmax	Number of peaks in normalised max spectral power over time.
64	p_peaksmaxmean	Ratio of peaks in normalised max vs mean spectral power over time.
65	p_peaksmaxmedian	Ratio of peaks in normalised max vs median spectral power over time.
66	p_peaksfcentral	Number of peaks over time at the central frequency.
67	p_diffmaxmean	Mean difference between max and mean power over time.
68	p_diffmaxmedian	Mean difference between max and median power over time.
69	p_diffquantile21	Mean difference between power quantiles 2 and 1 over time.
70	p_diffquantile32	Mean difference between power quantiles 3 and 2 over time.
71	p_diffquantile31	Mean difference between power quantiles 3 and 1 over time.
Signal-to-Noise Ratio (SNR) Features		
74	snr_B1	Signal-to-noise ratio in the 1–10 Hz frequency band (B1).
75	snr_B2	Signal-to-noise ratio in the 10–20 Hz frequency band (B2).
76	snr_B3	Signal-to-noise ratio in the 20–30 Hz frequency band (B3).

Continued on next page...

#	Feature Name	Definition
77	snr_B4	Signal-to-noise ratio in the 30–40 Hz frequency band (B4).
78	snr_B5	Signal-to-noise ratio in the 40–49 Hz frequency band (B5).
79	snr_B1_B2	Ratio of signal-to-noise ratios between the 1–10 Hz and 10–20 Hz bands ($\mathrm{SNR}_{B1}/\mathrm{SNR}_{B2}$).
80	snr_B3_B4	Ratio of signal-to-noise ratios between the 20–30 Hz and 30–40 Hz bands ($\mathrm{SNR}_{B3}/\mathrm{SNR}_{B4}$).
81	snr_B4_B5	Ratio of signal-to-noise ratios between the 30–40 Hz and 40–49 Hz bands ($\mathrm{SNR}_{B4}/\mathrm{SNR}_{B5}$).
82	snr_B1_B5	Ratio of signal-to-noise ratios between the 1–10 Hz and 40–49 Hz bands ($\mathrm{SNR}_{B1}/\mathrm{SNR}_{B5}$).
Spectral Mean Ratios Across Frequency Subranges		
83	s_mean1_2	Ratio of band-limited spectral mean: s_mean(1–15 Hz)/s_mean(15–30 Hz).
84	s_mean2_3	Ratio of band-limited spectral mean: s_mean(15–30 Hz)/s_mean(30–49 Hz).
85	s_mean1_3	Ratio of band-limited spectral mean: s_mean(1–15 Hz)/s_mean(30–49 Hz).
Station-Level Amplitude Feature		
86	rms_station	RMS amplitude of the (filtered) vertical component: $\sqrt{\mathrm{mean}(BHZ^2)}$.
Polarization and Particle-Motion Features		
87	rectilinearity	Rectilinearity from covariance eigenvalues ($\lambda_1 \leq \lambda_2 \leq \lambda_3$): $1 - \frac{\lambda_1+\lambda_2}{2\lambda_3}$.
88	azimuth	Azimuth (degrees) of the principal polarization direction from the dominant eigenvector: $\arctan\left(\frac{p_{2,3}}{p_{1,3}}\right) \cdot \frac{180}{\pi}$.
89	dip	Dip (degrees) of the principal polarization direction: $\arctan\left(\frac{p_{3,3}}{\sqrt{p_{2,3}^2+p_{1,3}^2}}\right) \cdot \frac{180}{\pi}$.
90	planarity	Planarity from eigenvalues: $1 - \frac{2\lambda_1}{\lambda_2+\lambda_3}$.
Fractal / Roughness Feature		
91	fractal_dimension	Fractal dimension estimated from the variogram scaling (Jaffar et al., 2024): compute variogram vs lag τ, fit slope on the first 4 points in log–log space, then $D = 2 - \frac{\mathrm{slope}}{2}$.

S1.3 Prominence Analysis

Prominence analysis identifies short-lived amplifications in a time-varying signal by quantifying how strongly local peaks rise above the surrounding background. Here, we apply this approach to the event–slip ratio.

The ratio is defined as

$$R_{\text{event-slip}}(t) = \frac{N(t)}{\Omega(t)}, \tag{A1}$$

where $N(t)$ is the cumulative number of detected seismic events and $\Omega(t)$ is the cumulative surface slip obtained by integrating the daily velocity time series $v(t)$, with $v(t) = \frac{d\Omega}{dt}$.

We estimate a slowly varying background of $R_{\text{event-slip}}(t)$ using a rolling linear regression over 7-day windows,

$$\hat{R}_{\text{event-slip}}(t_i) = \beta_0 + \beta_1 t_i, \tag{A2}$$

where $\hat{R}_{\text{event-slip}}(t_i)$ is the local background estimate at time t_i, and β_0 and β_1 are window-specific coefficients. Deviations from this background are defined as

$$\Delta(t) = R_{\text{event-slip}}(t) - \hat{R}_{\text{event-slip}}(t), \tag{A3}$$

which isolates short-term changes in seismic productivity relative to the local trend.

We apply prominence analysis to $\Delta(t)$ over intervals corresponding to rainfall episodes. For each interval, prominence is defined as

$$\text{Prominence} = \max[\Delta(t)]_{\text{rain}} - \mu_{\text{baseline}}, \tag{A4}$$

where $\max[\Delta(t)]_{\text{rain}}$ is the peak deviation during the rainfall period and μ_{baseline} is the mean deviation outside rainfall intervals.

S1.4 Quantification of Seismic Source Growth Rates

Let t denote continuous time and $\{t_i\}$ the occurrence times of detected seismic events. Cumulative seismicity is defined as

$$N(t) = \sum_{t_i \le t} 1, \tag{A5}$$

where $N(t)$ represents the total number of events that have occurred up to time t. The known failure time t_f is used only as a temporal reference (e.g., for visual alignment) and does not enter any fitting procedure.

To characterize short-term variations in seismic source activation, we quantify growth behaviour in moving windows of 300 consecutive events (step = 50 events). Within each window, we fit a finite-time power-law scaling to the cumulative counts:

$$\log N(t) = \alpha \log (t - t_0 + \varepsilon) + \beta, \tag{A6}$$

where

- α — local growth exponent (slope in log–log space), reflecting the rate of seismic source acceleration,
- β — intercept parameter for the log–log regression in the current window,
- t_0 — start time of the current window, establishing a finite-time reference,
- ε — small positive constant preventing singularity as $t \to t_0$.

We evaluate the stability of each α estimate using nonparametric bootstrapping: the 300 events are resampled 400 times and 95% confidence intervals are computed from each bootstrap ensemble.

We compute local growth exponents independently for the surface and subsurface seismicity domains, denoted

$$\alpha_{\text{surf}}(t), \qquad \alpha_{\text{sub}}(t),$$

based on $N_{\text{surf}}(t)$ and $N_{\text{sub}}(t)$, respectively.

To express their relative temporal dominance, we define the dynamic relative growth ratio

$$R_{\text{surf-sub}}(t) = \frac{\alpha_{\text{surf}}(t)}{\alpha_{\text{sub}}(t)}, \tag{A7}$$

where $R_{\text{surf-sub}}(t) > 1$ indicates stronger instantaneous growth of the surface source domain relative to the subsurface domain, and $R_{\text{surf-sub}}(t) < 1$ indicates the opposite. We propagate uncertainties from both $\alpha_{\text{surf}}(t)$ and $\alpha_{\text{sub}}(t)$ to obtain confidence bounds on $R_{\text{surf-sub}}(t)$. To highlight persistent temporal structure, we smooth $R_{\text{surf-sub}}(t)$ using a Savitzky–Golay filter.

S1.5 Bayesian Information Criterion (BIC)–Optimized Binary Segmentation

To detect temporal variations in seismic growth regimes, we apply binary segmentation to the $\alpha(t)$ time series using the `ruptures` Python package with an L2 cost function. The optimal number of change points k is selected by minimizing a Bayesian Information Criterion (BIC)–type score:

$$\mathrm{BIC} = \mathrm{cost} + \log(n)\,\mathrm{Var}(\alpha)\,k, \tag{A8}$$

where

- n — number of observations in the $\alpha(t)$ time series,
- cost — within-segment residual cost (sum of squared deviations from segment means),
- $\mathrm{Var}(\alpha)$ — empirical variance of the $\alpha(t)$ series,
- k — number of change points.

Minimizing Eq. (A8) balances model fit and complexity, yielding an optimal segmentation of the $\alpha(t)$ series and identifying major temporal transitions in seismic source growth dynamics. This approach was applied independently to the α_{sub}, α_{surf}, and $\alpha_{\mathrm{surf}}/\alpha_{\mathrm{sub}}$ time series.

S2 Results: Evaluation of detection and classification

In this section, we evaluate the performance of the machine learning models at each seismic station to assess their classification accuracy and robustness. We then compare the ML-based event detections with those obtained from Doppler radar to validate the reliability of the automated approach.

S2.1 Model Evaluation

BRZ02 demonstrated the highest classification accuracy across all event types, correctly identifying 94% of surface events, 88% of sub-surface events, over 99% of noise, and 98% of earthquakes. Misclassifications were minimal, largely arising between surface and sub-surface classes. BRZ03 maintained robust classification, though with slightly more confusion between classes. Earthquakes were classified with 76% accuracy, with 18% misclassified as surface events. Sub-surface and surface events were correctly identified 71% and 91% of the time, respectively. Noise remained well-separated, with over 93% accuracy. These results suggest that while BRZ03 benefits from relatively strong signal quality, site effects such as intermediate path attenuation and waveform distortion introduce moderate degradation in classification reliability. BRZ04 exhibited the lowest performance, particularly for earthquake and sub-surface categories. Earthquakes were correctly classified only 60% of the time, with significant confusion with surface and noise classes (25% and 15%, respectively). Sub-surface events showed 71% accuracy, while surface and noise events reached 84% and over 95% accuracy, respectively. This drop in performance is likely due to consistently lower signal-to-noise ratios at BRZ04, compounded by the fact that training labels derived from BRZ02 may not fully represent signal characteristics at this site. The F1 score analysis, which combines how often the model is right (precision) and how often it captures all relevant events (recall), shows that BRZ02—the primary station for labeling—achieved consistently high performance across all classes, with F1 scores of 0.99 (earthquake), 0.98 (noise), 0.96 (surface), and 0.93 (sub-surface), and demonstrated excellent stability, with standard deviations below 0.002 for surface and noise, and only minor variation for sub-surface ($\pm$0.019) and earthquake ($\pm$0.023) classes. BRZ03 showed similarly strong performance, with high mean F1 scores across all classes (0.96 for noise, 0.92 for surface, 0.85 for sub-surface), and low inter-fold variation. Despite limited high-quality training data, BRZ04 maintained reliable performance,

with mean F1 scores ranging from 0.73 (earthquake) to 0.93 (noise), and only slightly higher variability in the earthquake and sub-surface categories.

All manual labeling was performed using signals from BRZ02, which is located closest to the toe of the active rockslide. This proximity provided high-quality seismic recordings with excellent signal-to-noise ratios, making BRZ02 the most suitable reference station for training. In contrast, BRZ03 lies slightly farther upslope, and BRZ04 is situated on loose deposits from an older landslide, where signal attenuation and scattering are more pronounced—potentially reducing data quality and introducing local biases in the transferred labels. The performance of models BRZ03 and BRZ04 lags behind BRZ02, largely due to differences in signal quality between stations. As shown in the boxplot, the mean spectral power (s_mean) of both true positives (TP) and false positives (FP) is consistently lower (more negative) for BRZ03 and BRZ04 compared to BRZ02, indicating weaker signal amplitudes in both training and test samples. Specifically, BRZ03 and BRZ04 have median s_mean values below –130 dB, while BRZ02's median is closer to –125 dB for true positives. This lower signal-to-noise ratio likely contributes to a higher rate of classification errors at BRZ03 and BRZ04.

To evaluate ensemble voting performance, we reserve 20% of the BRZ04 dataset as a test set, ensuring representation of all event classes. The corresponding windows are then extracted from BRZ02 and BRZ03 to assemble a common test dataset shared across all stations. Each station-specific model is trained on the remaining 80% of its own dataset, and the trained models are subsequently applied to the shared test dataset. Their predictions are combined using the ensemble voting procedure to obtain the final network-level classifications. Performance is assessed by comparing individual model decisions with the ensemble consensus. The effects of individual misclassifications were effectively suppressed by ensemble voting, enabling robust classification across all seismic event classes with an overall accuracy of approximately 97.5%. Noise events were classified with exceptionally high accuracy (99.8%), reflecting strong separability from signal-based classes. Surface events were identified with high confidence (94.1%), with most misclassifications occurring in relation to noise. This overlap was likely driven by signal strength, as over 85% of the surface events misclassified as noise exhibited very low spectral power (s_mean ¡ –130 dB). This suggested that weak or degraded signals challenged the classifier's ability to distinguish surface activity from ambient noise. Sub-surface events achieved 97.5% accuracy, and earthquakes were classified with 88.1%, supported by a rule that bypassed ensemble voting when BRZ02 confidently identified an event as an earthquake—leveraging its demonstrated reliability for this class. Of the remaining misclassified events, approximately 10% were assigned to surface events, though this represented only a small fraction compared to the much higher frequency and dominance of true surface events in the dataset, suggesting that such misclassifications had limited impact on the overall surface event classification performance.

S2.2 Comparison with Doppler Radar

The Doppler-radar catalog (16 May–27 June 2023), originally acquired as part of the operational early-warning system for road closure and previously utilized in Schneider et al. (2023b); Kang et al. (2024a), was used here to evaluate the machine-learning-based seismic surface-event detections during the 15–17 June 2023 failure period, which was excluded from model training and validation. Because the seismic classifier operates using 50% overlapping sliding windows, a single radar-detected rockfall can produce multiple consecutive seismic detections. To account for this, consecutive seismic surface-event predictions (class = 3) were first collapsed into individual events using the 2 s sliding-window duration and subsequently merged when separated by gaps of $\leq$10 s, yielding a catalogue of unique seismic surface events. We then performed an event-level comparison by testing whether each of the 72 Doppler-radar events was associated with at least one high-confidence seismic surface-event prediction ($p \geq 0.7$) within $\pm$1 s of the radar

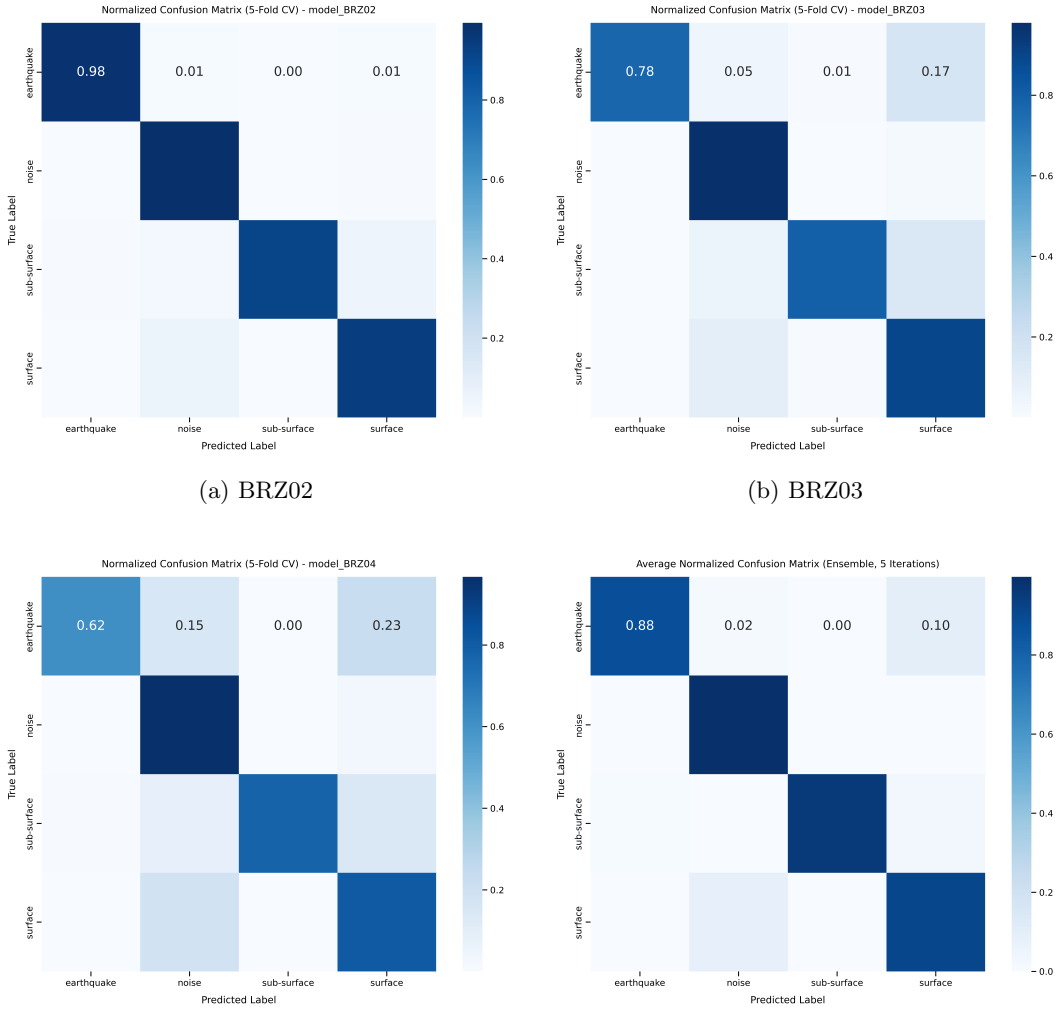

(a) BRZ02

(b) BRZ03

(c) BRZ04

(d) Ensemble

Figure S1: **Confusion matrices for individual stations and the ensemble.** Five-fold cross-validated, row-normalized confusion matrices for BRZ02, BRZ03, BRZ04, and the ensemble classifier.

onset time. The seismic models recovered nearly all Doppler events, with recall values of 98.6% for BRZ02, 97.2% for BRZ03, and 94.4% for BRZ04, demonstrating highly consistent detection performance across stations.

Outside the Doppler-radar event windows, the models identified additional unique seismic surface events, ranging from 1157 at BRZ02 to 2151 at BRZ04 after temporal merging. These unmatched detections likely represent small, short-duration rockfalls or localized surficial instabilities that remained below the effective detection or spatial-resolution threshold of the radar system. In addition, radar performance may have been reduced during the highly active pre-collapse phase because of overlapping motion, dust generation, and partial line-of-sight occlusion. Consequently, while the comparison demonstrates strong radar–seismic agreement for catalogued Doppler events, the seismic models also resolve a broader population of small-scale surface activity not fully captured by radar observations.

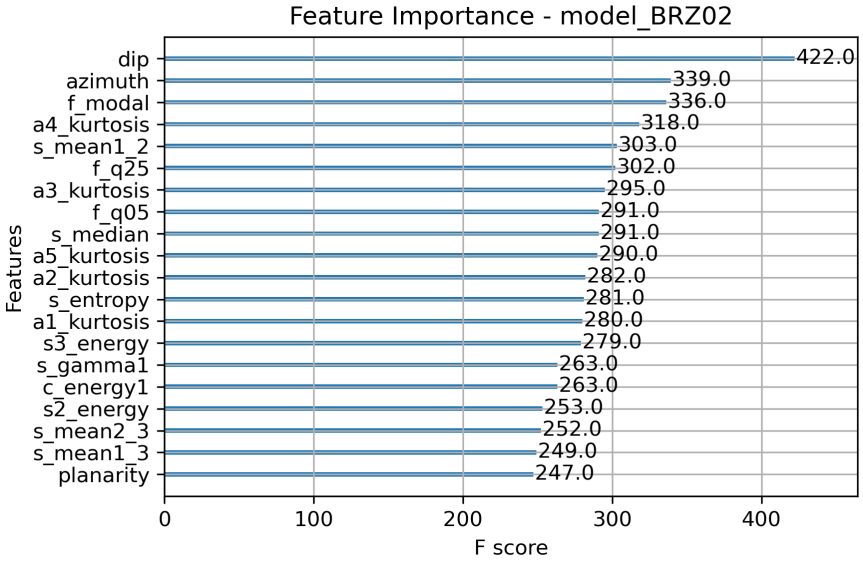

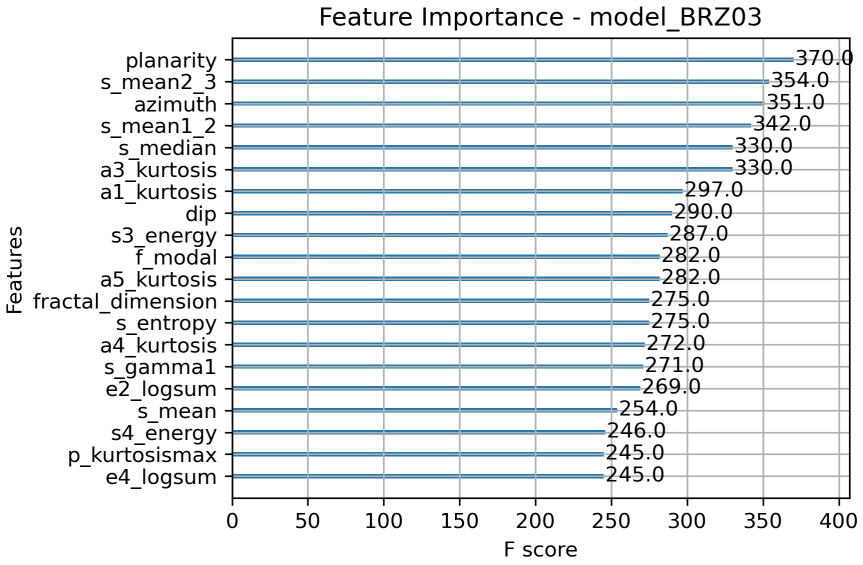

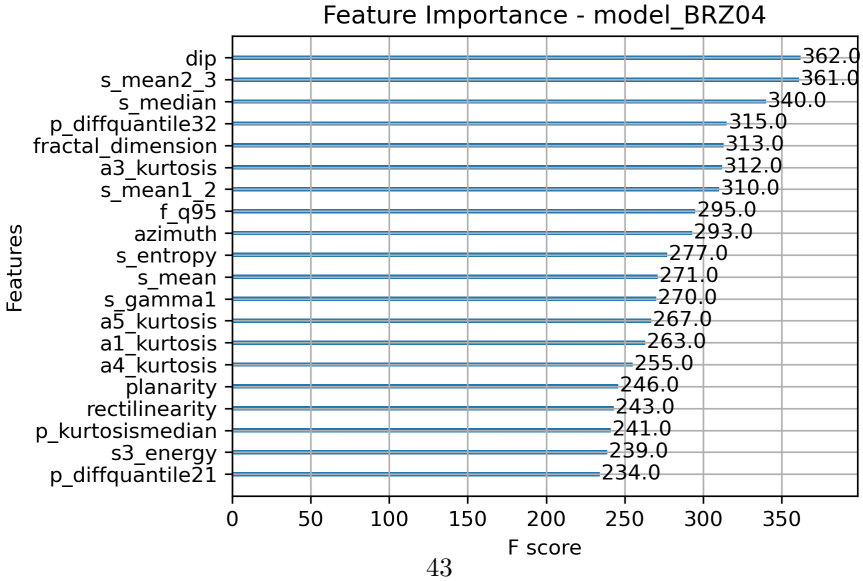

Figure S2: Feature importance rankings derived from the XGBoost classifiers for stations BRZ02, BRZ03, and BRZ04.

S2.3 Repeating Subsurface events

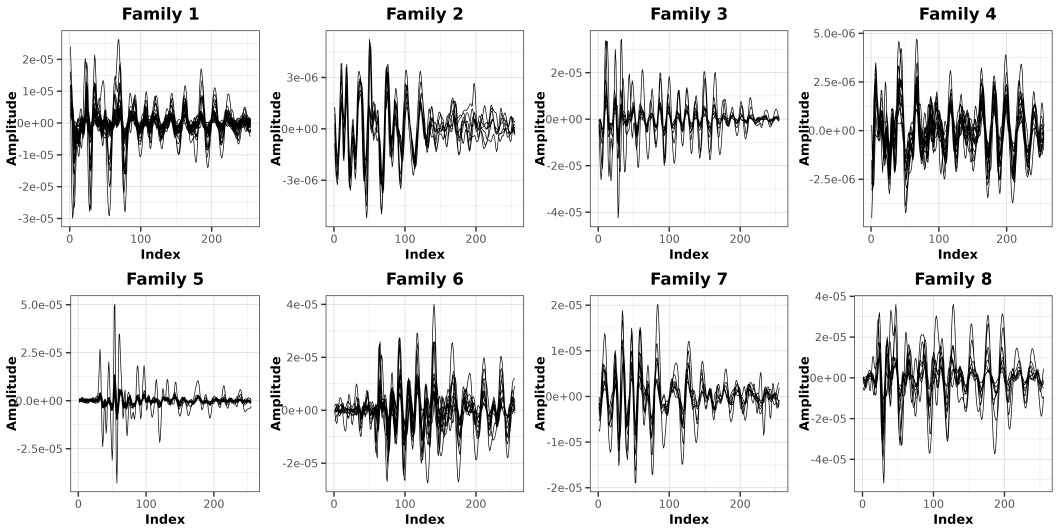

Figure S3: Spaghetti plots of the eight repeating event families identified in the STA–LTA event catalog using `REDPy`. A cross-correlation threshold of 0.8 was applied to group events into families. Each subplot corresponds to one family, showing the aligned member waveforms (component BHN, station BRZ02), highlighting the high waveform repeatability within each family.

S2.4 Correlation with Temperature

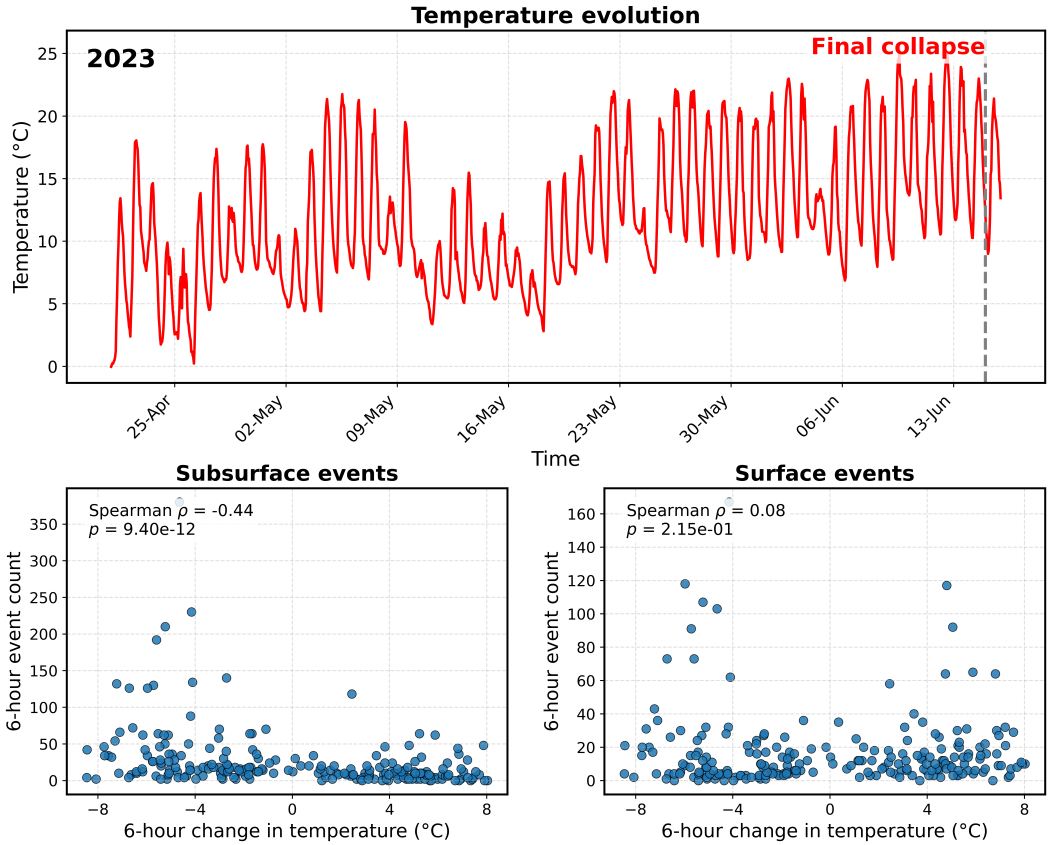

Figure S4: Temporal evolution of air temperature and its relationship with seismic activity at the Brienz/Brinzauls landslide between 21 April and 17 June 2023. The top panel shows hourly-averaged air temperature, with the timing of the final collapse (15 June 2023) indicated by a dashed vertical line. The lower panels present the relationship between 6-hour changes in temperature and corresponding 6-hour seismic event counts for (left) subsurface and (right) surface events. Subsurface seismicity exhibits a moderate negative monotonic relationship with temperature change (Spearman $\rho = -0.43$, $p \ll 0.01$), indicating increased activity during cooling phases. In contrast, surface seismicity shows no significant correlation with temperature variations (Spearman $\rho = 0.06$, $p = 0.33$).